Biogeosciences, 22, 4823–4849, 2025
https://doi.org/10.5194/bg-22-4823-2025
© Author(s) 2025. This work is distributed under
the Creative Commons Attribution 4.0 License.

Biogeosciences
Open Access
EGU

Research article

Can atmospheric chemistry deposition schemes reliably simulate stomatal ozone flux across global land covers and climates?

Tamara Emmerichs[1,a], Abdulla Al Mamun[2], Lisa Emberson[3], Huiting Mao[4], Leiming Zhang[2], Limei Ran[5], Clara Betancourt[6], Anthony Wong[7], Gerbrand Koren[8], Giacomo Gerosa[9], Min Huang[10], and Pierluigi Guaita[9]

[1]Institute of Energy and Climate Systems, Troposphere (ICE-3), Forschungszentrum Jülich, Jülich, Germany
[2]Air Quality Research Division, Science and Technology Branch, Environment and Climate Change Canada, Toronto, Ontario M3H 5T4, Canada
[3]Environment & Geography Department, University of York, York, UK
[4]Department of Chemistry, State University of New York College of Environmental Science and Forestry, Syracuse, NY, 13210, USA
[5]Soil science and Resource Assessment, National Resource Conservation Service, U.S. Department of Agriculture, Raleigh, NC 27609, USA
[6]AXA Konzern AG, Cologne, Germany
[7]Centre for Global Change Science, Massachusetts Institute of Technology, Cambridge, MA, USA
[8]Copernicus Institute of Sustainable Development, Utrecht University, Utrecht, the Netherlands
[9]Dept. of Mathematics and Physics, Catholic University of the Sacred Heart, Brescia, Italy
[10]Earth System Science Interdisciplinary Center, University of Maryland, College Park, MD, USA
[a]now at: Max Planck Institute for Meteorology, Hamburg, Germany

Correspondence: Tamara Emmerichs (tamara.emmerichs@gmx.de)

Received: 29 January 2025 – Discussion started: 14 February 2025
Revised: 24 June 2025 – Accepted: 26 June 2025 – Published: 22 September 2025

Abstract. Over the past few decades, ozone risk assessments for vegetation have evolved two methods based on stomatal O_3 flux. However, substantial uncertainties remain in accurately simulating these fluxes. Here, we investigate stomatal O_3 fluxes across various land cover types worldwide simulated by six established deposition models. Hourly O_3 concentration and meteorological data at nine sites were extracted from the Tropospheric Ozone Assessment Report (TOAR) database, a comprehensive global collection of measurements, for the model simulations. The models estimated reasonable O_3 deposition (0.5–0.8 cm s^{-1} in summer), which is mostly in agreement with the literature. Simulations of canopy conductance showed differences that varied by land cover type with correlation coefficients of 0.75, 0.80, and 0.85 for forests, crops, and grasslands among the models. Differences between models were primarily influenced by soil moisture and vapour pressure deficit, depending on each model's specific structure. Across models, the range of O_3 damage simulations at each site was most consistent for crops (6 to 11 mmol O_3 m^{-2}), followed by forests (3 to 19.5 mmol O_3 m^{-2}) and grasslands (7 to 33 mmol O_3 m^{-2}). The median estimate across models aligns well with the literature at the sites most vulnerable to O_3 damage. Overall, this study represents a critical first step in developing and evaluating tools for broad-scale assessment of O_3 impacts on vegetation within the framework of TOAR phase II.

1 Introduction

Elevated surface O_3 levels significantly damage vegetation due to the stomatal uptake of O_3 by canopy leaves. Stomatal uptake of O_3 leads to plant tissue injury, which in turn causes changes in metabolic functioning, reducing photosynthesis and consequently plant growth and productivity (Mills et al., 2011; Emberson, 2020; Ainsworth et al., 2012; Fuhrer et al., 2016; Grulke and Heath, 2020). Such damage can have significant impacts on crop yields and quality, leading to

economic losses and impacting food security in regions already facing scarcity (Avnery et al., 2011; Ainsworth, 2017; Ramya et al., 2023). There is an ever-growing body of observational evidence demonstrating a variety of O_3 impacts on different ecosystems (crops, forests, grasslands) in North America; Europe; and, more recently, Asia (Emberson 2020). Various indices assessing O_3 exposure to vegetation have been developed over recent decades, with the stomatal O_3 flux (POD_y; phytotoxic ozone dose over a threshold y) index found to provide better estimates of O_3 risk to vegetation than the more commonly used concentration-based exposure approaches (e.g. accumulated ozone over threshold (AOT); growing season daylight mean O_3 concentration (M7, M12), Mills et al., 2011; Avnery et al., 2011). A global overview of spatial distribution and trends using concentration-based metrics was provided in the first Tropospheric Ozone Assessment Report (TOAR) by Mills et al. (2018). During TOAR phase II (TOAR-II), we conduct a flux-based analysis to ensure the most up-to-date vegetation metrics are provided through this community effort.

O_3 dry deposition to vegetation is in part determined by canopy-level O_3 concentrations. A significant fraction of O_3 uptake occurs through the plant stomata with the remainder depositing on plant cuticular surfaces and the under-storey vegetation and soil. The stomatal contribution can vary between 50 % and 80 %, depending on the factors controlling the partitioning of stomatal and non-stomatal uptake (e.g. Huang et al., 2022; Wong et al., 2022; Clifton et al., 2023). As such, quantifying canopy stomatal conductance is important for assessing the mass balance of atmospheric O_3 concentrations and its potential damage to vegetation. Both stomatal and non-stomatal processes can vary with environmental conditions such as humidity, solar radiation, temperature, and CO_2 concentration as well as vegetation type and density (Clifton et al., 2020a). The occurrence of soil water deficit can also play a crucial role, where soil water stress induces stomatal closure (Li et al., 2020; Huang et al., 2022). There are two commonly used stomatal conductance (g_s) models – the empirical, multiplicative approach first developed by Jarvis (1976) and the semi-mechanistic coupled net photosynthesis–stomatal conductance models ($A_{net} - g_s$). The common Jarvis-type models (e.g. Emberson et al., 2000; Ganzeveld and Lelieveld, 1995; Zhang et al., 2003), widely applied due to their simplicity and computational efficiency, correct a prescribed maximum stomatal conductance with the multiplication of different environmental factors (e.g. temperature, light, soil water, and atmospheric moisture). The $A_{net} - g_s$ models couple g_s to plant photosynthesis by calculating the net assimilation of CO_2 and estimating g_s based on the resulting supply and demand of CO_2 (Farquhar et al., 1980; Goudriaan et al., 1985; Ball et al., 1987). $A_{net} - g_s$ models involve multiple non-linear dependencies on soil water, humidity, and temperature, among other factors defined by measurement constraints (Ball et al., 1987; Leuning, 1997). Heterogeneity of stomatal deposition estimates over different land cover types is anticipated, but model uncertainty depends on the representation of the deposition mechanisms, model parameterization, and meteorological inputs (Hardacre et al., 2015; Clifton et al., 2020b; Huang et al., 2022; Khan et al., 2025). Broadly speaking, the pros and cons of these two modelling approaches will tend to depend on the aims of the risk assessment study, the extent of knowledge of the ecosystem being investigated and prevailing bio-climatic conditions. Jarvis-type models are arguably more suitable for studies where less is known about the eco-physiology of the ecosystem since they do not require simulation of net photosynthesis, which in itself is inherently difficult to model accurately. However, these models still need to be calibrated for the particular bio-climate of study to ensure temperature and vapour pressure deficit (VPD) functions are suitable for the prevailing conditions. By contrast, $A_{net} - g_s$ models may be more useful for studies where the physiological response to environmental conditions of the ecosystems is reasonably well understood as they can provide insight into not only pollutant deposition but also how other environmental conditions in addition to pollution may limit plant growth and productivity more generally.

In this study, the stand-alone versions of six O_3 deposition schemes, commonly used in climate or air quality models, are assessed, with a focus on their stomatal uptake portion and resulting POD_y calculation. Using concurrent O_3 concentration and meteorological variable measurement data from the TOAR database enables us to conduct a detailed intercomparison of multiple deposition schemes by avoiding uncertainties arising from using different input data. For this study, various sites have been selected to represent different land cover types and climate regimes around the globe, focusing on sites where observational data are available for O_3 concentration. By assessing the model estimates of stomatal O_3 deposition at these different sites, we aim to identify key differences in model formulation and parameterization that influence estimates of stomatal O_3 flux and consequent POD_y. The estimation of the stomatal uptake from water flux measurements taken from the FLUXNET database provides an additional observational constraint as well as an uncertainty estimate at each site.

Furthermore, sensitivity simulations allow us to investigate the variability of stomatal O_3 deposition and plant damage with key input parameters and land cover characteristics. Post hoc, plant damage will be calculated offline based on the POD_y simulated by different models and flux–response relationships, where appropriate. Ultimately, we aim to understand the key factors driving stomatal O_3 flux and thus POD_y and assess the O_3-induced potential for vegetation damage for different land cover types and global regions.

2 Methodology

2.1 Meteorological and O_3 data from the TOAR-II database

The web version of the DO_3SE model is coupled to the TOAR database; i.e. the required input data (Table 3) are automatically provided by the database at the respective modelling sites. The TOAR-II database (from now on TOAR) contains harmonized measurements of surface O_3 and its important precursors and key meteorological variables that can impact O_3 concentrations and stomatal O_3 uptake. As one of the largest collections of quality-controlled air pollution measurements in the world, it comprises ground-based station measurements of O_3 concentration at more than 22 905 sites globally, which cover different periods between 1974 and 2023. These have been collected from different O_3 monitoring networks (e.g. Clean Air Status and Trends Network, CASTNET), harmonized and synthesized to enable uniform processing. The data were selected for inclusion in the TOAR database based on an extended quality control; e.g. sites where the measurement technique changed with time have been excluded. Data errors remain but have been shown to have a minor impact (Schultz et al., 2017). The total uncertainty in modern O_3 measurements is estimated to be $< 2\,\mathrm{nmol\,mol^{-1}}$ (Tarasick et al., 2019). The meteorological data (irradiance, air temperature, relative humidity, precipitation, air pressure, and wind speed) in the database stem from the fifth generation of ECMWF reanalysis (ERA5) for global climate (Hersbach et al., 2020). Data re-initialization (of precipitation and radiation, Copernicus Climate Change Service, 2017) is bridged by (linear) interpolation. The leaf area index (LAI) data in the database stem from the MODerate resolution Imaging Spectroradiometer (MODIS). TOAR data are freely and openly available through a graphical user interface and a representational State Transfer interface (https://toar-data.fz-juelich.de/api/v2/, last access: 1 November 2024). The TOAR data centre team is committed to the Findability, Accessibility, Interoperability, and Reusability principles (Wilkinson et al., 2016). The centre aims to achieve the highest standards regarding data curation, archival, and re-use (Schröder et al., 2021). To conduct offline simulations with models in addition to Web-DO_3SE, the input data were extracted beforehand and proven for identicality. The additionally required data (Table 3) were extracted from the TOAR database and the MeteoCloud server (https://datapub.fz-juelich.de/slcs/meteocloud/index.html, last access: 21 September 2024) at Forschungszentrum Jülich.

2.2 Observation-constrained stomatal conductance

To compare the modelled stomatal conductance with observational information, we prepared model input data at two sites (Hyytiälä, Harvard Forest) from the FLUXNET 2015 dataset (Pastorello et al., 2020), which is openly available under the CC-BY-4.0 data usage license. Additional vegetation information for the model input (i.e. LAI, canopy height, and crop calendar data) was provided by the site project investigators. Then, we used the canopy-scale stomatal conductance dataset, SynFlux version 2, to estimate G_{st} for two forest sites, US-Ha1 and FI-Hyy. While in SynFlux version 1, canopy transpiration is assumed to be equal to total latent heat flux, SynFlux version 2 improved its previous estimations (Ducker et al., 2018) using a machine-learning-based method (Nelson et al., 2018) to partition total evapotranspiration into surface evaporation and canopy transpiration. To train quantile random forest models to relate meteorological conditions with water use efficiency (derived from water and carbon fluxes), periods with minimal surface wetness were chosen during the growing season. These models were then used to back-calculate transpiration for the whole growing season. Instead of the total latent heat flux, the resulting transpiration estimate was used as an input to the inverse Penman–Monteith equation, reducing the potential high bias in the stomatal conductance estimates in SynFlux version 1.

2.3 Summary of sites selected for deposition modelling

Nine sites (Table 1) were selected for this modelling work accounting for the following factors: (i) geographical spread, including major continents with terrestrial vegetation; (ii) land cover/use types, including the plant functional types (PFTs) which are important in terms of economy, food security, or biodiversity and for which we have fairly good knowledge of O_3 impacts; (iii) availability of meteorological and O_3 data from the TOAR database; (iv) availability of observational data describing stomatal conductance of water vapour (g_{wv}) estimated from the FLUXNET measurements (Sect. 2.2); and (v) location proximity to previous experiments that have investigated O_3 impacts on vegetation that can help interpret our model results.

2.4 Stomatal deposition models and their key inputs

Six widely used empirical/Jarvis and semi-empirical/Ball–Berry types of stomatal deposition models were selected for this study. All of these used models can accommodate a variety of land cover/land use types and provide estimates of stomatal deposition that can be output as both hourly- and season-long cumulative-stomatal deposition metrics. The key model features are described below.

1. The empirical/Jarvis-type models use a predefined stomatal conductance modified with different environmental stressors for radiation (PAR), air temperature (T), vapour pressure deficit (VPD), and soil water (SM): the ZHANG model (Zhang et al., 2002, 2003) and the Web-DO_3SE model (i.e. a version of DO_3SE that is directly coupled to the TOAR database, Emberson et al., 2000) account for sunny and shaded leaves (two big

Table 1. Sites selected for stomatal deposition modelling using data from the TOAR database grouped by continent. Sites that also have FLUXNET data are denoted by "FN", and those with SynFlux data are denoted by "SF".

Site (TOAR station ID, nearest FLUXNET site ID)	Location, station altitude from TOAR	Köppen–Geiger climate classification	Vegetation details (LAI, canopy height in m)	Record (measurement heights in m)	References
Europe					
Hyytiälä, Finland (FI00621, FI-Hyy) FN & SF	61.8611° N, 24.2833° E; 104 m	Dfc	LAI: 2.9 Height: 23.3	O_3: 2014 (4) FLUXNET: Apr 1996–Sep 2013 (14)	Chen et al. (2018); Junninen et al. (2009); Visser et al. (2021)
Grignon, France (FR04038, FR-Gri) FN	48.5819° N, 1.833° E; 165 m	Cfb	LAI: 4.3 Height: 3.5	O_3: 2013/2014 (3) FLUXNET: 2004–2014 (2)	Stella et al. (2013)
Castelporziano, Italy (IT0952A, IT-Cpz)	41.8894° N, 12.266° E; 19 m	Csa	LAI: 6.9 Height: 14.0	O_3: 2013/2014 (19.7) FLUXNET: 2013/2014 (10)	Gerosa et al. (2005, 2009), Fares et al. (2009, 2012), Silvano Fares (personal communication, 2024)
Asia					
Amberd, Armenia (AM0001R)	40.3844° N, 44.2605° E; 2080 m	BSk (or Dfa)	LAI: 3.9 Height: 1.0	O_3: 2009/2010 (3)	
Pha Din, Vietnam (VN0001R)	21.5731° N, 103.5157° E; 1466.0 m	CWA	LAI: 6.9 Height: > 10.0	O_3: 2015–2017 (12)	Pieber et al. (2023), Bukowiecki et al. (2018), Yen et al. (2013)
North America					
Quabbin Reservoir/Harvard Forest tower, USA (25-015-4002, US-Ha1) FN & SF	42.2985° N, −72.3341° E; 312 m	Dfb	LAI: 3.0 Height: 24.0	O_3: 2010–2012 (2) FLUXNET: 1993–2012 (24)	Clifton et al. (2019, 2020b), Ducker et al. (2018)
Nebraska, USA (31-055-0032, US-Ne3)	41.3602° N, −96.0250° E; 400 m	Dfa	LAI: 1.7 Height: 2.5	O_3: 2010 (2) FLUXNET: April 2013– (0.5)	Amos et al. (2005), Leung et al. (2020)
South America					
Huancayo, Peru (PE0001R)	−12.0402° N, −75.3209° E; 3314 m	Cwb	LAI: 3.6 Height: 1.0	O_3: 2015 (6)	
Africa					
Mt. Kenya, Kenya (KE0001G)	−0.062° N, 37.297° E; 3678.0 m	Aw	LAI: 4.2 Height: 1.0	O_3: 2015 (unknown)	Henne et al. (2008a, b)

Table 2. Land cover type, species, and growing season (where SGS: start of growing season and EGS: end of growing season) by site. The equivalent land cover type and soil texture data used by the models used in this study (Sect. 2.3) are also shown. MESSy does not consider different land cover types. Models that do not consider soil type (i.e. do not include an estimate of soil moisture influence on stomatal deposition) are marked with *.

Station site: land cover type (species) and growing season	Web-DO_3SE	TEMIR*	NOAH-GEM	ZHANG*	CMAQ
Hyytiälä, Finland: evergreen needleleaf forest (Scots pine) SGS = 1, EGS = 366	evergreen needleleaf forest, loam	evergreen needleleaf boreal forest	evergreen needleleaf forest, organic material	evergreen needleleaf forest	evergreen needleleaf forest, silty loam (peat)
Grignon, France: crops (rapeseed and wheat) SGS = 304, EGS = 571	winter wheat, loam	C_3 crop	crops/grassland mosaic, silt loam	crops	crops (wheat), silty loam
Castelporziano, Italy: evergreen broadleaf forest (laurel, abutus, broad-leaved phillyrea, holm oak, pine) SGS = 1, EGS = 366	evergreen broadleaf forest, loam	Evergreen broadleaf temperate forest	evergreen broadleaf forest, sandy loam	evergreen broadleaf forest	evergreen broadleaf forest, loamy sand
Amberd, Armenia: Grassland, mixed SGS = 1, EGS = 366	grassland, loam	grassland	grassland, loam	long grassland	grassland, loam
Pha Din, Vietnam: evergreen needleleaf forest SGS = 1, EGS = 366	evergreen needleleaf forest, loam	evergreen needleleaf temperate forest	evergreen needleleaf forest, clay	evergreen needleleaf forest	evergreen needleleaf forest, clay
Quabbin Reservoir/ Harvard Forest tower, USA: SGS = 93, EGS = 312	temperate mixed forest, loam	deciduous broadleaf temperate forest	deciduous broadleaf forest, sandy loam	deciduous broadleaf forest	deciduous broadleaf forest, sandy loam
Nebraska, USA: crops (maize/soybean rotation) SGS = 132/148, EGS = 278/260	crops (maize, soybean), loam	C_3 crop	crops/grassland mosaic, silty clay loam	crops	crops (corn), silty clay loam
Huancayo, Peru: grassland SGS = 1, EGS = 366	grassland, loam	grassland	grassland, loam	long grassland	grassland, loam
Mt. Kenya, Kenya: grassland, shrublands SGS = 1, EGS = 366	grassland, loam	grassland	grassland, loam	long grassland	grassland, silty loam

leaves), and the Web-DO_3SE model also depends on the vegetation phenology. The CMAQ_J model (Pleim and Ran, 2011) and the MESSy model (Ganzeveld and Lelieveld, 1995; Kerkweg et al., 2006) account for one big leaf. CMAQ_J uses relative humidity (RH) instead of VPD. MESSy calculates the initial stomatal conductance based on the PAR and several empirical parameters.

2. Semi-empirical/Ball–Berry: the CMAQ_P model (Ran et al,. 2017) and the TEMIR model (Collatz et al., 1991; Farquhar et al., 1980) calculate the stomatal conductance at sunlit and shaded leaves for C_3 and C_4 plants depending on the net CO_2 assimilation rate, CO_2 partial pressure, atmospheric pressure (Pa), and water vapour pressure for each leaf. The NOAH-GEM model is different, calculating stomatal conductance for one big leaf

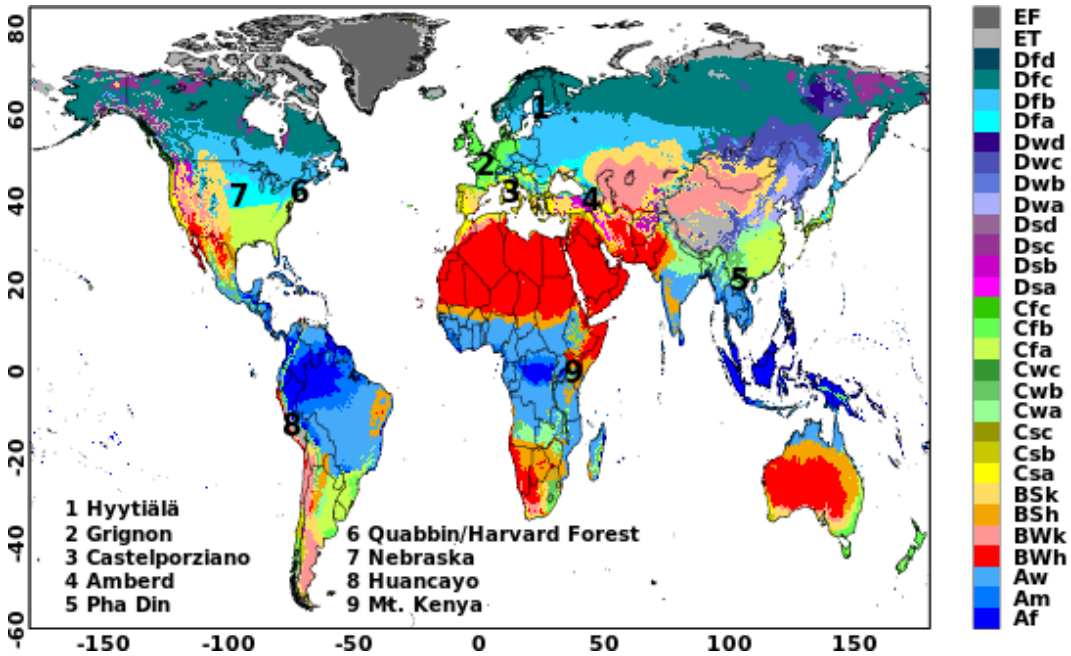

Figure 1. Locations of nine selected sites on Köppen–Geiger climate classification map for 1991–2020 (source: Beck et al., 2023). Table 1 specifies the classifications of these sites. Publisher's remark: please note that the above figure contains disputed territories.

using RH instead of VPD (Wu et al., 2011; Niyogi et al., 2009).

All models follow the resistance scheme.

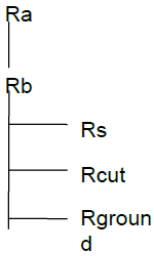

The land cover, growing season, and soil texture specifications used by the models are summarized in Table 2. For crops, we used the GGCMI Phase 3 crop calendar (Jägermeyr et al., 2021a), which provides the planting date and maturity day for 18 different crops at a 0.5° land grid cell resolution (Jägermeyr et al., 2021b). For forest trees, we consider four various classes: evergreen needleleaf (EN), evergreen broadleaf (EB), deciduous needleleaf (DN), and deciduous broadleaf (DB). For evergreen species, we assume a year-round growing season; for deciduous species, we use the simple latitude function described in Hayes et al. (2007); and we consider a year-round growing season for tropical species. The soil texture categories used by the models were obtained from the reference studies in Table 1 and the site principal investigators. Table 3 provides the key formulas, input data requirements, and references for all models. Key total and stomatal deposition parameters for empirical models ($g_{\max}$) and semi-empirical models ($V_{C_{\max}}$) are described in Table 4, which gives a good indication of the overall difference in the magnitude of stomatal deposition. The models' meteorological and O_3 inputs have been introduced in Sect. 2.1.

POD_y is calculated in post-processing, according to the guidelines in UNECE LRTAP (2017):

$$POD_y = \sum_{i=1}^{n} \left[\mathrm{fst}, \mathrm{sun}_i - y \right] \times \left(\frac{3600}{10^6} \right)$$
$$\text{for } \mathrm{fst}, \mathrm{sun}_i \geq y \,\mathrm{nmol\,m^{-2}\,PLA\,S^{-1}}, \quad (1)$$

where $\mathrm{fst}, \mathrm{sun}_i$ is the hourly mean O_3 flux in $\mathrm{nmol\,O_3\,m^{-2}\,PLA\,s^{-1}}$ at sunlit leaves, y is a species-dependent threshold (crops: $6\,\mathrm{nmol\,O_3\,m^{-2}\,s^{-1}}$, grassland and forests: $1\,\mathrm{nmol\,O_3\,m^{-2}\,s^{-1}}$; UNECE LRTAP, 2017), and i is the number of daylight hours (when ssrd $> 50\,\mathrm{W\,m^{-2}}$) within the accumulation period (growing season). The term $(3600/10^6)$ converts from $\mathrm{nmol\,m^{-2}\,PLA\,s^{-1}}$ to $\mathrm{mmol\,O_3\,m^{-2}}$ PLA. fst, sun is calculated by

$$f_{\mathrm{st,sun}} = c\frac{(z) \times g_{\mathrm{st}} \times r_{\mathrm{c}}}{r_{\mathrm{b}} + r_{\mathrm{c}}}, \quad (2)$$

where $c(z)$ is the O_3 concentration at in $\mathrm{nmol\,m^{-3}}$, calculated from ppb by multiplying by P/RT, where P is the atmospheric pressure (Pa), T is the air temperature (K), R is the universal gas constant of $8.31447\,\mathrm{J\,mol^{-1}\,K^{-1}}$, and T is the assumed standard air temperature (293 K). The leaf surface resistance (r_{c}) is given by $r_{\mathrm{c}} = 1/(g_{\mathrm{st}} + g_{\mathrm{ext}})$, where g_{ext} is the inverse of cuticular resistance.

Table 3. Stomatal deposition models selected for site-scale modelling (list of symbols: A1 and Sect. S3 in the Supplement, * uses $u(h)$, $o3(h) = 1$, for US-Ne: $u(h)$, $o3(h) = 0.3$).

Model	Approach	Key formulas	Key input data	Reference
ZHANG	Empirical (Jarvis-style)	$R_s = \frac{1}{\left[G_s(\mathrm{PAR}) f(T) f(D) f(\psi) \times \frac{D_i}{D_v}\right]}$ $G_s(\mathrm{PAR}) = \frac{L_{sun}}{r_s(\mathrm{PAR}_{sun})} + \frac{L_{shade}}{r_s(\mathrm{PAR}_{shade})}$ $r_s(\mathrm{PAR}) = r_{s,min}\left(1 + \frac{b_{rs}}{\mathrm{PAR}}\right)$	LAI, LUC, Wspeed, ssrd, T2m, Tskin, RH	Zhang et al. (2002, 2003, 2006)
Noah-GEM	Semi-empirical, photosynthesis-based (Ball–Berry type)	$R_s = 1/\left[\mathrm{LAI}\left(\frac{m A_n h_s P}{C_s} + b\right)\right]$	LAI, LUC, Wspeed, ssrd, strd, T2m, Tskin, RH	Wu et al. (2011), Niyogi et al. (2009)
CMAQ_J	Empirical (Jarvis-style)	$R_s = \frac{r_{s,min}\mathrm{LAI}}{(f_{\mathrm{PAR}} f_T f_{\mathrm{vpd}} f_w)}$	LAI, T_{air}, PAR, ssrd, rn, RH SM	Pleim and Ran (2011)
CMAQ_P	Semi-empirical, photosynthesis-based (Ball–Berry type)	$R_s = 1/\left(\frac{m_g A_{net} e_s P_a}{C_s} e_i + g_0\right)$	LAI, CO_2, Pa, $u*$, h_dis, $z0$, SM, T_{soil}, wspeed, wdir, soil texture, C_3/C_4 type, PAR, ssrd, rn, P_rate, sn, sd	Ran et al., 2017
TEMIR	Semi-empirical, photosynthesis-based (Ball–Berry type)	$R_s = \frac{1}{\left[\left(\frac{L_{sun}}{r_b + r_{sun}} + \frac{L_{shade}}{r_b + r_{shade}}\right)\frac{D_i}{D_v}\right]}$ $r_s = \frac{1}{g_s} = \frac{1}{\left[\alpha\left(\frac{m A_n\left(\frac{e_s}{e_{sat}}\right)}{\left(\frac{C_s}{P_{atm}}\right)} + b\right)\right]}$	LAI, LUC, $u*$, ssrd, T2m, Tskin, RH, SM	Tai et al. (2024), Sun et al. (2022)
MESSy	Empirical (Jarvis-style)	$R_s = \left[r_s(\mathrm{PAR}, \mathrm{LAI}) \mid f_T f_{\mathrm{vpd}} f_w\right] \times \frac{D_v}{D_i}$ $r_s(\mathrm{PAR}, \mathrm{LAI}) = kcx$ $\left[\frac{b}{\mathrm{dPAR}} \ln\left(\frac{\exp(k\mathrm{LAI})+1}{d+1}\right) - \ln\left(\frac{\exp(-k\mathrm{LAI})}{d+1}\right)\right]^{-1}$	LAI, ssrd, RH, sw, Tir	Emmerichs et al. (2021), Kerkweg et al. (2006) Ganzeveld and Lelieveld (1995)
Web-DO_3SE	Empirical (Jarvis-style)	$r_s = g_{max} \max\left\{\left(f_{min}, f_{temp}, f_{VPD}, f_{SWC}\right)\right\} \times f_{phen} \times f_{light}$	T_{air}, VPD wspeed, P, Pa, O_3, Gr	Emberson et al. (2000), Büker et al. (2012), Simpson et al. (2012), Guaita et al. (2023)

The leaf boundary resistance is calculated by

$$r_b = 1.3 \times 150 \times \sqrt{\frac{L}{u(h)}}, \quad (3)$$

where factor 1.3 accounts for the differences in diffusivity between heat and O_3, L is the crosswind leaf dimension (i.e. leaf width in m), and $u(h)$ is the wind speed at the top of the canopy.

2.5 Description of stomatal deposition model simulations

The result section aims at identifying trends in stomatal deposition models among different land cover types including grass, crops, and forests using four model experiments as follows.

In experiment 1, the different models are driven by the O_3 and meteorological data from ERA5. We analysed the simulated deposition velocity (V_d) split into stomatal and non-stomatal fractions, canopy (G_{st}) and sunlit (G_{sun}) stomatal conductance.

To include observational constraints, in experiment 2, the TEMIR, ZHANG, NOAH, MESSy, and CMAQ models were run with data obtained from the FLUXNET database (available for three sites; see Table 1), and the simulated G_{st} was evaluated with observation-derived values, inferred G_{st}, of SynFlux. Spearman correlation was applied for the model evaluation, as it can be applied to any datasets including non-parametric and non-linear ones. The US-Ha1 and FI-

Table 4. Model parameter $V_{C_{max}}$ at standardized temperature conditions (25° C) [in µmol CO_2 m^{-2} s^{-1}] and g_{max} [O_3 in cm s^{-1}] for the total canopy by land cover/land use type. Note that the values presented in the table were recalculated from the original respective rsmin values for H_2O (s m^{-1}) in ZHANG, MESSy, and CMAQ_J and $V_{c_{max}}$ values for O_3 (mol O_3 m^{-2} s^{-1}) in Web-DO_3 SE.

Parameter	Web-DO_3SE	ZHANG	CMAQ_J	TEMIR	NOAH-GEM	CMAQ_P
G_{max} or $V_{C_{max}}$	g_{max} [cm s^{-1}]	g_{max} [cm s^{-1}]	g_{max} [cm s^{-1}]	$V^{+}_{C_{max}}$ [µmol CO_2 m^{-2} s^{-1}]	$V_{C_{max}}$ [µmol CO_2 m^{-2} s^{-1}]	$V_{C_{max}}$ [µmol CO_2 m^{-2} s^{-1}]
Forests	0.44 (EN) 0.49 (EB) 0.55 (DB)	0.25 (EN) 0.42 (EB) 0.42 (DB) Zhang et al. (2003)	0.36 (EN), 0.53 (EB), 0.32 (DB), Pleim and Ran (2011)	60.1 (EN) 59.0 (EB) 55.4 (DB), Oleson et al. (2013), NCAR Technical notes	57.6 (EN) 96 (EB) 96 (DB) Niyogi et al. (2009), JAMC	57.6 (EN, Ran et al., 2017), 49.2 (EB, Medi. forest, (EB_tr + EB_te)/2, Ran et al., 2017), 55.4 (DB, CLM4.5, Kattge and Knorr, 2007)
Crops	1.1 (wheat) 0.74 (maize) 0.73 (soybean)	0.53	0.91	96.7	76.8	96.7 (CLM4.5)
Grasses	0.66	0.64	0.64	75.1	28.8	75.1 (CLM4.5)

Hyy sites were considered for the model evaluation due to the availability of SynFlux data at these sites.

A sensitivity analysis (experiment 3) was performed by driving a set of models with synthetic input data in the following steps: (i) O_3 input was perturbed by ±40 % (Sofen et al., 2016). (ii) Soil water content was perturbed by ±30 % (Li et al., 2020). (iii) Absolute humidity was perturbed by ±30 %, and soil and air temperatures were perturbed by ±3, independently. (iv) The growing season, which was mostly approximated by LAI, was shifted by 14 d forward and backward in time. In set (iii) and (iv), relative humidity was calculated from absolute humidity and temperature after their perturbation. In both cases, absolute humidity was capped at the saturation vapour pressure at the corresponding temperature.

Finally, for experiment 4, g_{max} and $V_{C_{max}}$ of the models were varied by ±20 %, based on previous estimates of plant-trait-dependent uncertainty (e.g. Walker et al., 2017; UNECE LRTAP, 2017).

3 Results

3.1 General characteristics of simulated total deposition velocity and stomatal contribution

The split of total O_3 deposition between different pathways, G_{st}, G_{cut}, and G_{ground}, simulated by the seven models, is shown for each of the nine sites in Figs. 2 and S2 (corresponding data are presented in Table S9). This analysis allows us to briefly assess the overall efficacy of the model's ability to simulate deposition velocity V_d (by comparisons with previously published values; more complete assessments of model's ability for some of these sites can be found in Clifton et al., 2023) and to compare the importance of the stomatal deposition pathway between models for different land cover types and across different seasons.

Observations of V_d have only been made at a handful of sites, i.e. Hyytiälä, Finland; Castelporziano, Italy; Grignion, France; and Harvard Forest, USA (close to our Quabbin site in terms of proximity, land, cover type and climate). Overall, the models capture V_d at these sites compared to observed values reported in previous studies. Namely, the observed seasonal cycles in V_d at Hyytiälä, Finland (needleleaf forest), with lows of ~ 0.1 cm s^{-1} between January and April and highs of 0.4 cm s^{-1} between June and September, averaged over 10 years of measurements from Clifton et al. (2023) and Visser et al. (2021) are captured by most models except MESSy and TEMIR, which reach V_d values of 0.8 cm s^{-1} during the summer. Similarly, the strong seasonal cycle in V_d at Quabbin, USA (temperate mixed forest), ranging from around 0.2 cm s^{-1} between January and April up to 0.5 cm s^{-1} from June to September in Clifton et al. (2023), is captured by all models. Observed V_d at Castelporziano, Italy (evergreen broadleaf forest), shows relatively

constant values throughout the year, commonly between 0.4 and 0.8 cm s^{-1} averaged over a 2-year period (Savi and Fares, 2014). The study by Stella et al. (2011) reports V_d measurements of 0.63 cm s^{-1} (on average) at Grignion (France). At the other sites, no O_3 dry deposition measurement exists, and thus we report the observed ranges for the land cover type (and possibly the matching climate). Over grassland, Silva and Heald (2018, and references therein) show a mean of 11 measurements of daytime V_d values ($\sim$ 0.4 cm s^{-1}) in agreement with our models. Measurements exist at soybeans and maize crops which indicate V_d values of 0.7 (Meyers et al., 1998) and 0.4–0.6 cm s^{-1} (Stella et al., 2011), respectively. Thus, the models seem to estimate too low deposition at soybeans.

In terms of deposition pathways, for all sites and models, stomatal deposition consistently ranks as the most important pathway in the summer, whereas in winter and, for some models, in the autumn G_{st} decreases to zero to very low at sites with seasonal variation in vegetation coverage. The importance of the pathway varies with land cover type and season. The highest stomatal contribution of 90 % (NOAH model) is shown at the Amberd site. Among the different land cover types, the highest average stomatal contribution to deposition during the summer is estimated across grass (67 %), followed by crops (65 %) and forests (59 %). The seasonal importance of stomatal contribution is not seen for the tropical sites as the year-round growing season means that stomatal conductance is driven by solar radiation, which is constant throughout the year (e.g. Hardacre et al., 2015). Previous studies involving measurements and partitioning approaches (Horváth et al., 2018; Mészáros et al., 2009) indicate that the non-stomatal O_3 deposition pathways (i.e. G_{ground} and G_{cut}) are very strong (in some cases, dominant over G_{st}) at short vegetation such as the grasslands. Despite there being multiple factors, such as wind speed, solar radiation, and LAI, which control the relative contributions of the three deposition branches, G_{st} is the dominant pathway at the three grassland sites of the current study (Amberd, Mt. Kenya, and Peru). At the Amberd and Peru sites, G_{cut} and G_{ground} are small since low wind speed reduces downward mixing of ozone to the surface (atmospheric resistance; e.g. at the Peru site in the summer season, the mean wind speed was 1.0 cm s^{-1}, and the G_{cut} and G_{ground} contributions in the TEMIR model were 21 % and 12 %, respectively; Table S3).

In contrast, at the Mt. Kenya site, G_{st} exceeds G_{cut} and G_{ground}, since the strong solar radiation (annual mean is 246 W m^{-2}, Table S2) at this site favours stomatal opening. Besides that, LAI is a very important governing factor for G_{st}. Therefore, it can be inferred that the O_3 deposition pathway depends on not only the land cover type but also meteorological drivers. The relative contribution of each deposition pathway depends on the interplay between these key factors at a particular site. Among the models, Web-DO_3SE estimated the lowest stomatal contribution at grass (Fig. 2) most likely due to its parallel pathways to cuticle, soil, and stomata, with the former scaled by LAI with a constant cuticular deposition of 2500 s m^{-1}. Such differences in model structures likely led to the wide-ranging partitioning. For example, for the Quabbin site (summer), all models simulate G_{cut} ranging from 15 %–65 %, G_{ground} from 2 %–19 %, and G_{st} from 33 %–66 % despite their agreement on the overall V_d values (total bar). Models agree better in the partitioning of O_3 dry deposition to crops, with summer stomatal fraction contributions ranging between 46 %–73 %, 37 %–73 %, and 51 %–81 % for US-Ne3 Maize, US-Ne3 soybeans, and FR-Gri (rapeseed and wheat). Most models estimate non-stomatal deposition equal to or larger than the stomatal contribution to deposition outside of the tropics in winter and autumn and to some extent in spring. This again emphasizes the importance of the stomatal contribution to the seasonal cycle of total deposition as also found in Clifton et al. (2023). Similarly, as seen at grasslands, Web-DO_3SE (Fig. 2, Table S3) accounts for the highest non-stomatal deposition at crop sites.

Across all forest sites, models show significant cuticular uptake throughout the year ranging between 11 % and 94 % contribution. At FI-Hyy, G_{cut} averages $\sim$ 50 % across all seasons and all models with higher estimates of $\sim$ 55 % by the TEMIR model due to the higher wind speed at FI-Hyy (annual mean wind speed is 3.2 m s^{-1}; Table S2), favouring cuticular deposition as suggested by Rannik et al. (2012). At IT-Cpz, our models estimate on average around 43 % (20 %–80 %) to be non-stomatal deposition, close to the previously reported ranges (Gerosa et al., 2005; Fares et al., 2012, 2014), which were up to 57 % from non-stomatal deposition and 30 %–60 % from stomatal uptake. A similar partitioning (59 % G_{st}, 33 % G_{cut}, 5 % G_{ground} model average in summer) is seen at PhaDin.

All models except Web-DO_3 SE were compared on a seasonal and hourly basis with the SynFlux G_{st} data for US-Ha1 and FI-Hyy sites (Figs. S2, S3). CMAQ_J, NOAH, TEMIR, and ZHANG show reasonable agreement at the Quabbin forest (US-Ha1), whereas CMAQ_P and MESSy show quite significant overestimates at both FI-Hyy and Harvard Forest (Table S5) and CMAQ_J overestimates at FI-Hyy only. Note that NOAH and ZHANG show significant underestimates at FI-Hyy while agreeing well with SynFlux at Harvard Forest (Quabbin). The underestimates by the ZHANG model are consistent with the results from a similar comparison for Yellowstone National Park in the USA by Mao et al. (2023). Compared to Harvard Forest, FI-Hyy is the most humid and cloudy with the lowest solar radiation flux, and these conditions likely contribute to the underestimates by the NOAH and the ZHANG model as identified by Mao et al. (2023). The differences between modelled and SynFlux G_{st} do not seem to be associated with the model types, i.e. empirical or photosynthesis-based models.

The correlation of the diurnal cycle of G_{st} calculated by the models with the inferred G_{st} by SynFlux for US-Ha1 and FI-Hyy (Fig. S4) confirms that models generally capture the

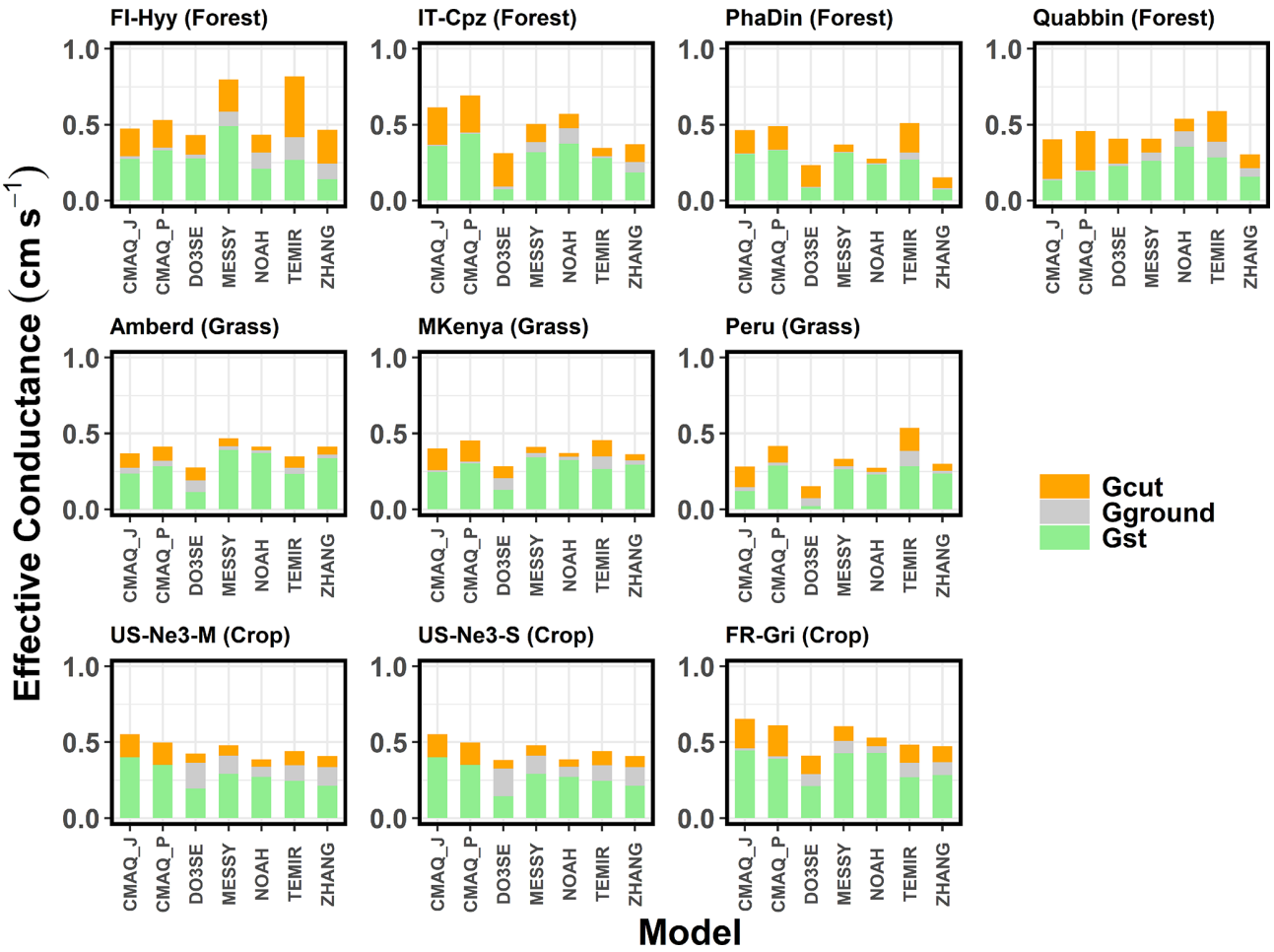

Figure 2. Mean effective conductance of the cuticular (G_{cut}), ground (G_{ground}), and stomatal (G_{st}) deposition pathways of O_3 across various models and sites during the summer season (US-Ne3-S = soybeans, US-Ne3-M = maize). Respective figures for the other seasons are presented in the Supplement.

temporal patterns of G_{st} of at least these two different forest types and climates (FI-Hyy: EN, temperate, subarctic; Quabbin: DB, moist temperate). The best Spearman correlations are found at FI-Hyy and range between 0.73 by the MESSy model and 0.85 by the TEMIR model. Overall lower correlations are found at the Quabbin site ranging from 0.65 for the NOAH and MESSy models to 0.82 for the CMAQ_P model. This poorer correlation suggests that additional water stress may limit stomatal conductance at Quabbin, which the models do not capture, compared to FI-Hyy. Notably, a similar range of correlation coefficients (0.61–0.93) was found when modelled G_{st} values obtained using the TOAR input data were compared with SynFlux G_{st}. As SynFlux data were generated using FLUXNET measurement data, this result corroborates the validity of using the TOAR database as input to Web-DO$_3$SE, developed as a service website to aid in risk assessment of O_3 damage to European vegetation.

To identify the key drivers of the G_{st} model schemes among different land cover types and climate conditions, we also compare estimates of G_{st} between models for all sites and analyse the similarity of G_{st} diurnal cycles in empirical and photosynthesis models. Here, it is important to understand the model distinction between shaded and sunlit leaf (G_{sun}, Fig. 4). The average diurnal variations of stomatal conductance (G_{st}) of O_3 at the 9 sites for each season are shown in Figs. 3 and S7. This also helps interpret the modelled stomatal conductance of sunlit leaves (G_{sun}) shown in Figs. 4 and S8. Across all models, the diurnal mean G_{st} (Fig. 3) varied from 0.15 cm s^{-1} (Quabbin) to 0.50 cm s^{-1} (Mt. Kenya). In the TEMIR and the ZHANG model, roughly 50 % of G_{st} occurs at the sunlit part of the leaves. Web-DO$_3$SE and CMAQ_P G_{sun} contribute 30 % on average (Fig. 4). At middle to high latitudes, the model spread is limited to the summer season, whereas at tropical sites, it is similar throughout the year. During the day, models show a spread of 1.2 cm s^{-1} in G_{st} at the forest and grassland sites during the summer, while their predictions agree most at the crop sites (throughout the year) with a maximum

of $1.0\,\mathrm{cm\,s^{-1}}$. This is due to the flux–response relationship, which has a more sensitive response (steeper slope for most crops) due to a higher threshold (see Table 5 for the equations describing the steepness of the change). Results among the same model type differed significantly, while different model types could produce similar results at the same location. For the sites with distinct seasonal variations, model differences were the largest in summer.

In comparison, TEMIR and ZHANG, photosynthesis-based and Jarvis-style, respectively, are both governed mainly by solar radiation (see higher G_{sun} in Fig. 4), showing close agreement, except in summer, at the forest sites (ZHANG values are very low). Only these two show a midday depression in G_{sun} at the peak of solar radiation at Mt. Kenya (the site with the highest radiation). The ZHANG model also estimated this feature for G_{sun} and G_{st} at other grassland sites (Figs. 3 and 4). This feature could be due to the day length (seasonality) scaling of $V_{C_{\max}}$ in TEMIR, causing G_{st} to increase significantly during summer at higher-latitude sites. In contrast, at lower-latitude sites (Mt. Kenya and Huancayo, Peru), the seasonal variation in day length is smaller, and there is subsequently smaller seasonality in $V_{C_{\max}}$ and G_{st}. The TEMIR and the CMAQ_P models, both photosynthesis-based, estimate very similar G_{sun} values (Fig. 4) at PhaDin (autumn, winter), IT-Cpz (spring, summer), and FI-Hyy (summer), whereas the G_{st} estimates show significant differences. The opposite occurs at Quabbin, where the G_{sun} values of the two models differ much more than the G_{st} estimates. These results illustrate that the different fractionations between shaded and sunlit leaves could mainly contribute to the model spread in stomatal conductance.

Further examination of individual models' features can shed light on the causes of model/site differences in G_{st}. The MESSy G_{st} value is strongly governed by LAI followed by soil moisture, and in all other respects MESSy treats different land cover types the same. Therefore, MESSy simulates the highest G_{st} values at PhaDin, Grignion, and Mt. Kenya, with LAI values of 6.9, 4.3, and $4.2\,\mathrm{m^{-2}\,m^{-2}}$, respectively (Table 1). In contrast to PhaDin, the high LAI site IT-Cpz ($6.9\,\mathrm{m^{-2}\,m^{-2}}$) experiences significant water stress during summer. This is only captured by MESSy and NOAH, indicating higher sensitivity to water stress. During the day, an evident midday depression of G_{st} due to hot weather and water shortage is seen, accompanied by a peak in the early morning evident from NOAH, the same as what has been observed in Mediterranean ecosystems (e.g. Gerosa et al., 2005). The NOAH model accounts for the direct effect of relative humidity on G_{st} (see model description in the Supplement) and subsequently modelled a depression in G_{st} at the daily onset (08:00 a.m. LT). This variation explains the G_{st} peak at IT-Cpz and Quabbin, which are, especially in the summer, the two driest among all sites. Due to the dry conditions at the Quabbin site, low soil water, and low relative humidity, most models, except NOAH, simulate the lowest summer daily mean G_{st} values among all sites. The high estimate by the NOAH model can be explained by the highest $V_{C_{\max}}$ value among the photosynthesis models (Table 4). The high $g_{\max}$ value of $0.55\,\mathrm{cm\,s^{-1}}$ used in Web-DO$_3$SE leading to large estimates is largely dampened by strong soil moisture stress at IT-Cpz (Table S2). Similarly, Web-DO$_3$SE estimates the lowest G_{st} (among the models) values at the Peru site (grassland) due to a strong limitation by the f_{temp} function on stomatal conductance, suggesting that the minimum temperature for stomatal opening at 12 °C is too low for these cool temperate conditions. The ZHANG estimates are generally governed by $g_{\max}$, explaining the highest and lowest G_{st} values of all models simulated with the ZHANG model at grassland and forest sites, respectively. The CMAQ_J model has the lowest $g_{\max}$ values, but it is strongly impacted by soil moisture. The additional dependence of the ZHANG model on solar radiation is reflected in higher G_{sun} relative to G_{st} (Figs. 3 and 4). TEMIR also simulates the smallest spread of G_{st} among the three grassland sites (Ambred, MKenya, Peru), as temperature acclimation of photosynthesis (Kattge and Knorr, 2007) is implemented. The different temperatures among the three sites have smaller effects on photosynthetic capacity and G_{st} than other models. Despite explicitly considering soil water stress, TEMIR does not capture the impacts of water stress on G_{st} in IT-Cpz and Quabbin in the summer, as the equivalent soil moisture threshold to trigger soil water stress at IT-Cpz and Quabbin is very low ($< 0.1\,\mathrm{m^{-2}\,m^{-3}}$). Both versions of CMAQ respond very strongly to soil moisture, which may not be accurate for each site. The differences between CMAQ-J and CMAQ-P are greatest at the sites with the greatest LAI, such as IT-Cpz and PhaDin.

The difference between total and sunlit stomatal flux is examined, and trends of stomatal sunlit flux are characterized by different land cover types and climate conditions. Figures 5 and 6 show the (SRAD $> 50\,\mathrm{W\,m^{-2}}$) stomatal O$_3$ flux (F_{st}) and stomatal, sunlit O$_3$ flux ($F_{\mathrm{st,sun}}$) for different models per season at nine sites representing forest (top), grass (middle), and crops (bottom). Thereby, we consider whether G_{st} and O$_3$ concentration co-variate at diurnal and seasonal timescales. Across all land cover types, a large range of F_{st} (0.05–2 $\mathrm{ppb\,m\,s^{-1}}$, Fig. 5) is estimated, usually highest in spring and summer and lowest in winter. The largest median of F_{st} is found at Amberd ($0.75\,\mathrm{ppb\,m\,s^{-1}}$; ZHANG, summer), followed by IT-Cpz ($0.60\,\mathrm{ppb\,m\,s^{-1}}$; NOAH, spring), and FR-Gri ($0.60\,\mathrm{ppb\,m\,s^{-1}}$; MESSy and NOAH, summer), owing to both higher G_{st} and O$_3$ concentrations at the respective sites (Fig. 3). Consequently, no general trend can be identified among the sites; i.e. flux estimates can differ within one land cover type. Namely, the two crop sites show very different F_{st} estimates (Fig. 5) since they have the most different O$_3$ levels across one land cover type. The FR-Gri site is exposed to an annual mean O$_3$ of 45 ppb (Table S1); the lowest O$_3$ level is 25 ppb among all sites. The same applies for the diurnal variation of O$_3$, causing either a high (FR-Gri)

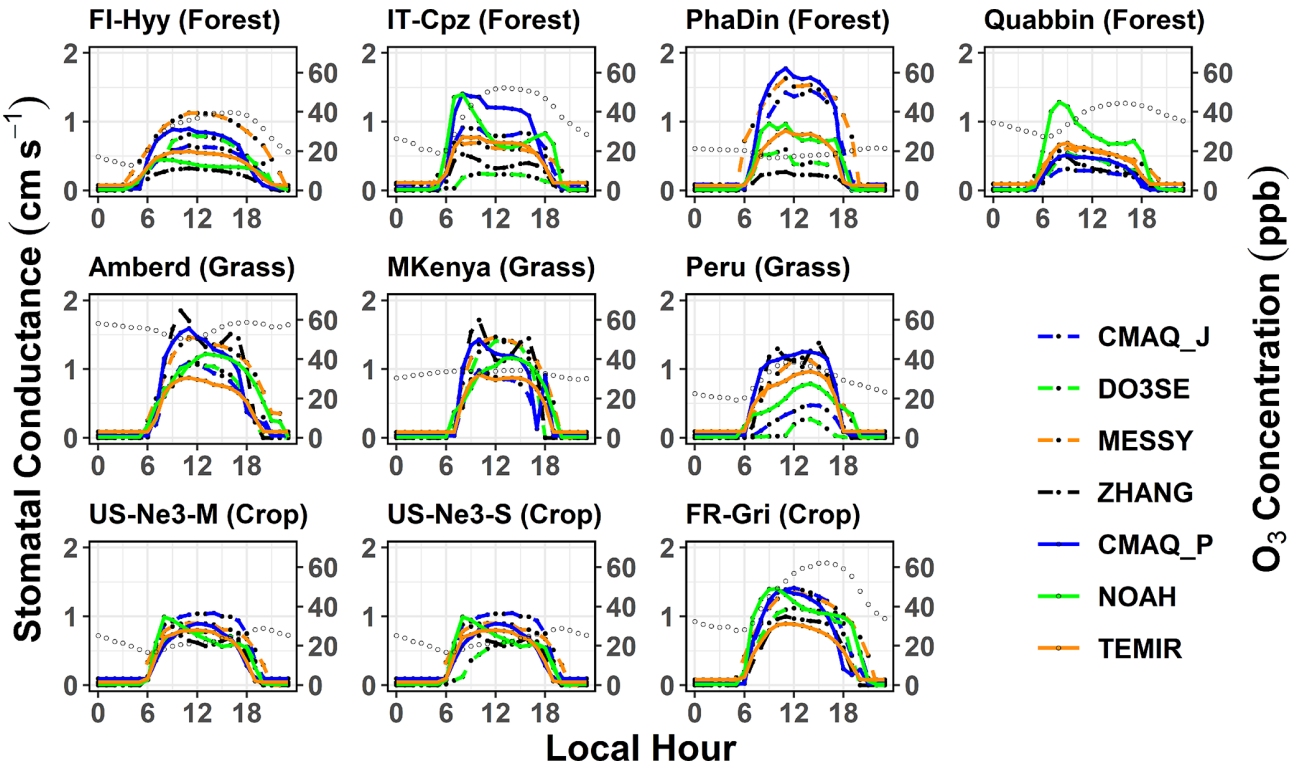

Figure 3. Mean diurnal cycle of total stomatal conductance (G_{st}) from models across various sites during the summer season (US-Ne3-S = soybeans, US-Ne3-M = maize). Open circles indicate diurnal O_3 variations. Respective figures for the other seasons are presented in the Supplement.

or a low range (US-Ne3) of flux estimates among all models (in summer and spring). The difference is less apparent in the $F_{st,sun}$ estimates (Fig. 6) which point to the sensitivity of the two leaves to O_3 concentration. Similarly, as seen for the stomatal conductance, three of four models show a very good agreement of F_{st} and $F_{st,sun}$ among each other. In terms of seasonality, models agree also generally well among the grassland sites. Among those (and all land cover types), the maximum annual median $F_{st,sun}$ was estimated for Amberd attributed to the high daytime (07:00 a.m.–07:00 p.m. LT) annual O_3 concentrations (49.3 ppb, Table S1). The most different $F_{st,sun}$ (and $F_{st,sun}$) values are found between the ZHANG (highest) and Web-DO$_3$SE model (lowest) due to the difference in G_{sun} (Fig. 4). Web-DO$_3$SE disagrees the most with the other models and predicts very small fluxes at the Peru site following the small G_{st} and G_{sun} values (Figs. 3 and 4).

Among forest sites, spring $F_{st,sun}$ values are comparably high as summer fluxes following the seasonal variation of G_{sun} (Fig. 6, outside the tropics). The highest spring estimates at PhaDin and Quabbin (forests) are linked to the site-specific yearly O_3 maximum in this season (Fig. 3). The flux seasonal maximum is more pronounced in all four models (ZHANG, CMAQ_P, TEMIR) when the O_3 concentration variation during the year is larger at the respective site. The highest $F_{st,sun}$ (0.1 ppb m s^{-1}) is estimated by TEMIR at PhaDin (spring), reflecting the high G_{sun} estimate. In contrast, when considering the total F_{st}, CMAQ_P shows the highest estimate (Fig. 5), which indicates that TEMIR uses a higher sunlit fraction than CMAQ_P, as has been shown for stomatal conductance (Figs. 3 and 4). The difference is most apparent at high LAI sites (PhaDin, IT-Cpz, FR-Gri). The lowest estimates of $F_{st,sun}$ (and a very small spread) at the forest sites are shown by the ZHANG model, as has been explained for G_{st} and G_{sun}. Overall, CMAQ_P has the lowest spread among the models, which was also found in the multi-model comparison study by Clifton et al. (2023).

3.2 Vegetation impact and variation with key input data

This section presents the POD$_y$ calculated from the O_3 deposition by different models at nine different stations to identify trends and patterns of POD$_y$ among land cover types and climates (Fig. 7, corresponding data in Table S9). The critical threshold for ozone damage y differs for the three land cover types. For forests and grass the y value is 1 nmol O_3 m^{-2} s^{-1} (POD$_1$), while O_3 damage to crops is assumed to occur only when the y threshold exceeds 6 nmol O_3 m^{-2-1} (POD$_6$). By driving the models with changed input data of O_3, soil moisture, temperature, relative humidity, and growing season (Fig. 8) and with changed $V_{c_{max}}/g_{max}$ parameter (Fig. 9), we

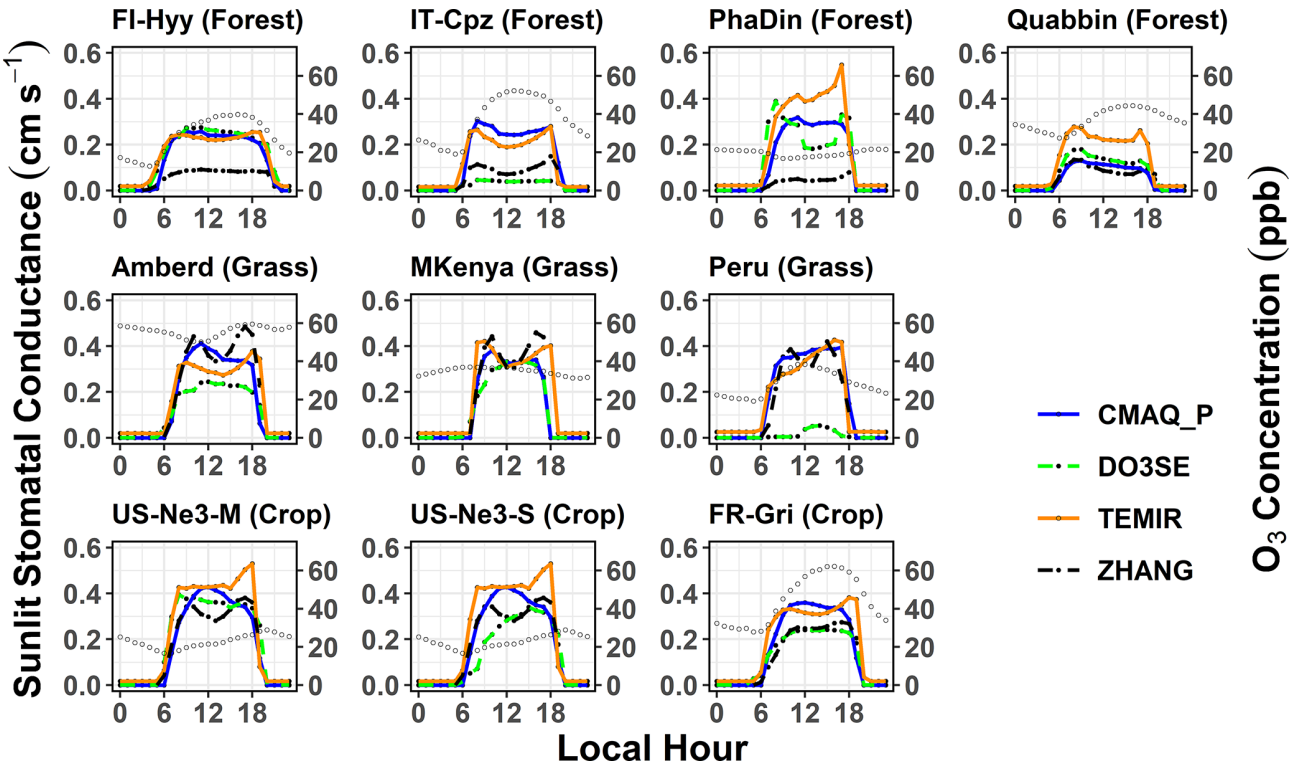

Figure 4. Mean diurnal cycle of leaf-level sunlit stomatal conductance (G_{sun}) from the three two-leaf models (CMAQ_P, TEMIR, and ZHANG) across various sites during the summer season (US-Ne3-S = soybeans, US-Ne3-M = maize). Open circles indicate diurnal O_3 variations. Respective figures for the other seasons are presented in the Supplement.

explore the sensitivity of the POD_y estimates. As shown in the previous analysis, the largest O_3 uptake and thus the highest POD_y of 28 mmol O_3 m^{-2} (on average among all models) is estimated over grassland sites (compared to forest and crops) (Fig. 7). POD_1 increases linearly with time for evergreen grasslands, whereas Mt. Kenya shows the fastest accumulation (due to the highest F_{st} in spring and summer). Three of the four models lie in a range of 5 mmol O_3 m^{-2}, whereas Web-DO$_3$SE predicts a maximum POD_y of 10 mmol O_3 m^{-2} at all grassland sites. Only at the Peru site can these low values be explained by the significantly lower G_{sun} and $F_{st,sun}$ (compared to other models).

For forests, our modelled ensemble POD_1 median and maximum values (ranging between 8 and 25 mmol O_3 m^{-2}) are similar in scale to values estimated across broad geographical regions by other studies. Karlsson et al. (2025) estimated POD_1 values across Europe with the highest values in mid-latitude Europe for coniferous (15 to 20 mmol O_3 m^{-2}) and broadleaf (22 to 28 mmol O_3 m^{-2}) forests. However, the ZHANG and the Web-DO$_3$SE model are estimated to obtain significantly lower POD_1 than CMAQ_P and TEMIR at each site. These estimates average to 16 mmol O_3 m^{-2}. There is no obvious pattern to which models tend to estimate higher or lower POD_1 values, but these estimates are generally consistent with G_{sun} (Fig. 4) and $F_{st,sun}$ (Fig. 6) model estimates explained by particular model constructs or parameterizations. For instance, the ZHANG model estimates low stomatal deposition and thus also POD_y over all forests. Web-DO$_3$SE saw a low O_3 uptake only due to the site conditions at IT-Cpz.

For crops, the model estimates of POD_6 are a little more consistent, with modelled differences within sites only varying between ∼ 3 and 11 mmol O_3 m^{-2}; however, this could in part be due to the overall lower POD_6 values due to the use of the higher y threshold. Median model ensemble values range between ∼ 7 and 12 mmol O_3 m^{-2} across sites. POD_6 for staple crops has been estimated in other studies across Europe and globally. A European study (Schucht et al., 2021) on wheat found POD_6 values of up to ∼ 4 mmol O_3 m^{-2} suggesting that our POD_6 values for the FR-Gri site tend to be too high. Feng et al. (2012) estimated maximum POD_6 values of up to 8 mmol O_3 m^{-2} for winter wheat in China, though these higher values are likely driven by higher ozone concentrations. Similarly, Wang et al. (2022) also found POD_6 values for maize of up to 8 mmol O_3 m^{-2}. Our models give the largest range in POD_6 estimates for soybeans at the US-Ne3 site (0 to 11 mmol O_3 m^{-2}). A key determinant of the range in POD_y simulated by our models, and also with estimates provided in the literature, is the value chosen for g_{max} (or $V_{C_{max}}$ depending on the model construct). For

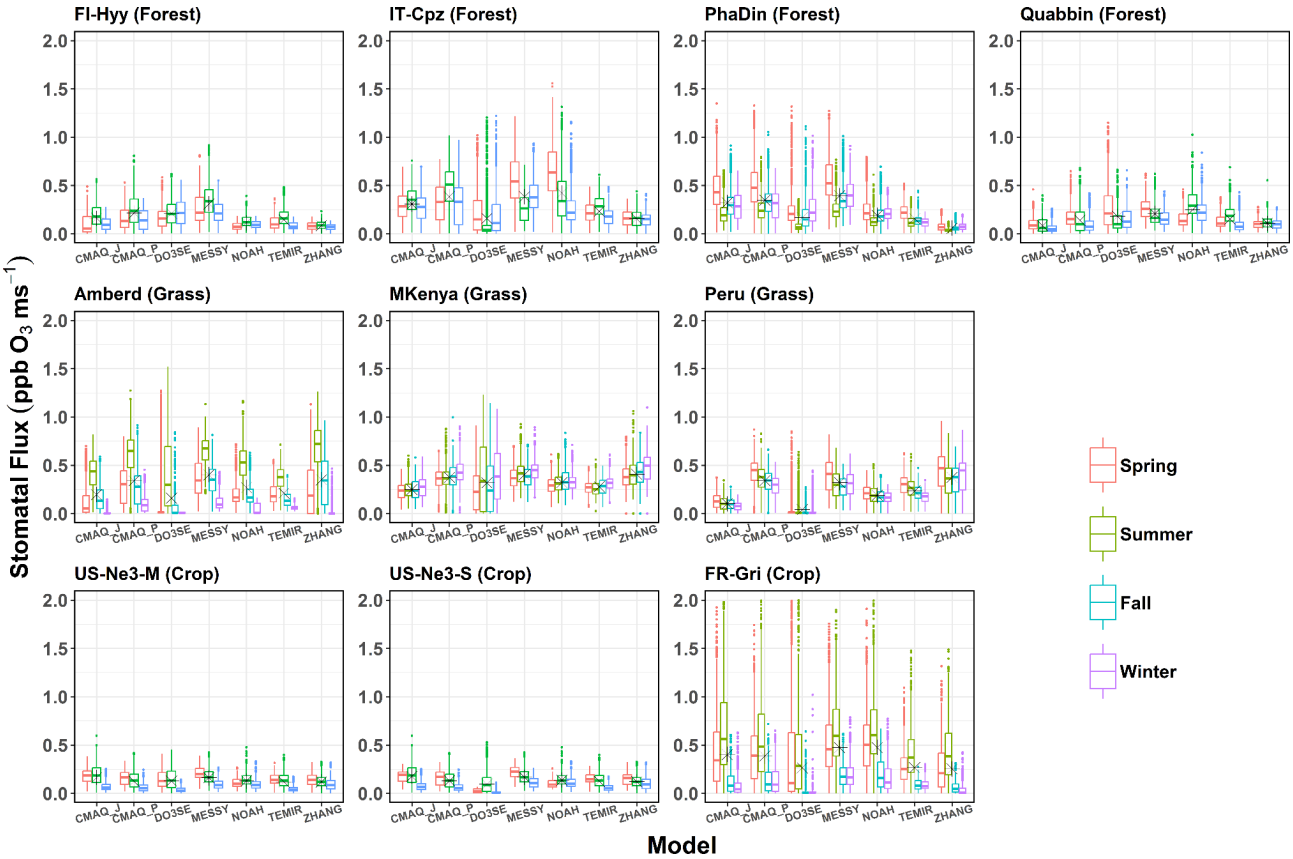

Figure 5. Box plots of seasonal mean canopy-level total stomatal O_3 flux (ppb O_3 m s^{-1}) for different models across various sites (data represent SRAD > 50 W m^{-2} and the growing period). Asterisks indicate the annual mean flux.

example, the multiplicative g_{sto} models used to derive flux–response relationships (see Table 5) use g_{max} values of 450, 126, and 301 mmol O_3 m^{-2} s^{-1} for wheat, maize, and soybeans (UNECE LRTAP, 2017; Peng et al., 2019; Zhang et al., 2017). By contrast, our modelling uses a variety of g_{max} values; for example, the Web-DO$_3$SE model uses 450, 305, and 300 mmol O_3 m^{-2} s^{-1} for wheat, maize, and soybeans. A further consideration in parameter selection is local conditions; a study by Stella et al. (2013) found a g_{max} value of 296 mmol O_3 m^{-2} s^{-1} was most appropriate to describe wheat g_{sto} at the FR-Gri site. This variation highlights the importance of selecting appropriate model parameterization for conditions, as well as consistency of parameterization with models used to develop flux–response relationships.

From the sensitivity analysis, we found that all models show sensitivity of POD$_y$ to changes in O_3, specific humidity, and temperature with varying degrees over different land cover types, possibly due to different prescribed values such as the temperature threshold (Fig. 8, corresponding absolute values in Table S10). In particular, the POD$_y$ at all sites is most significantly changed when modifying the O_3 concentration by ±40 % (Table S11). Crop is the most sensitive land cover to O_3 changes across the different models (8.5 mmol m^{-2}; 76 % POD$_y$ change with respect to the base run), followed by forest (10.0 mmol O_3 m^{-2}; 59.3 %) and grass (14.9 mmol O_3 m^{-2}; 56.1 %), which is due to the plant physiognomy (Grulke and Heald, 2020). In a relative sense, the average response change in POD$_y$ to a 40 % change in O_3 concentrations is the greatest in ZHANG (+9.2 mmol O_3 m^{-2}, corresponding to a 68.1 % POD$_y$ change with respect to the base run), followed by CMAQ_P and TEMIR (12 and 11.9 mmol O_3 m^{-2}; 64.8 % and 63.5 %), and then by Web-DO$_3$SE (11.4 mmol O_3 m^{-2}; 53.0 %). Also, the POD$_y$ estimate seems to be sensitive to humidity (Q) changes (±30 %) among all models. At forest, the POD$_y$ estimates appear to be the most sensitive (4.6 mmol O_3 m^{-2}; 27.3 %), followed by crops (2.9 mmol O_3 m^{-2}; 25.9 %) and grass (4.6 mmol O_3 m^{-2}; 17.3 %). The response is the greatest in TEMIR and CMAQ (between 5.7 and 6.7 mmol O_3 m^{-2}; 30.7 %–35.8 %), while it is much smaller for ZHANG (usually close to zero on average). The most non-linear response was shown by Web-DO$_3$SE at IT-Cpz, which estimated a 5 times higher POD$_y$ response to increasing humidity than to a humidity decrease, pointing towards the strong dryness at this site limiting factor. If temperature is changed by ±3 K the highest sen-

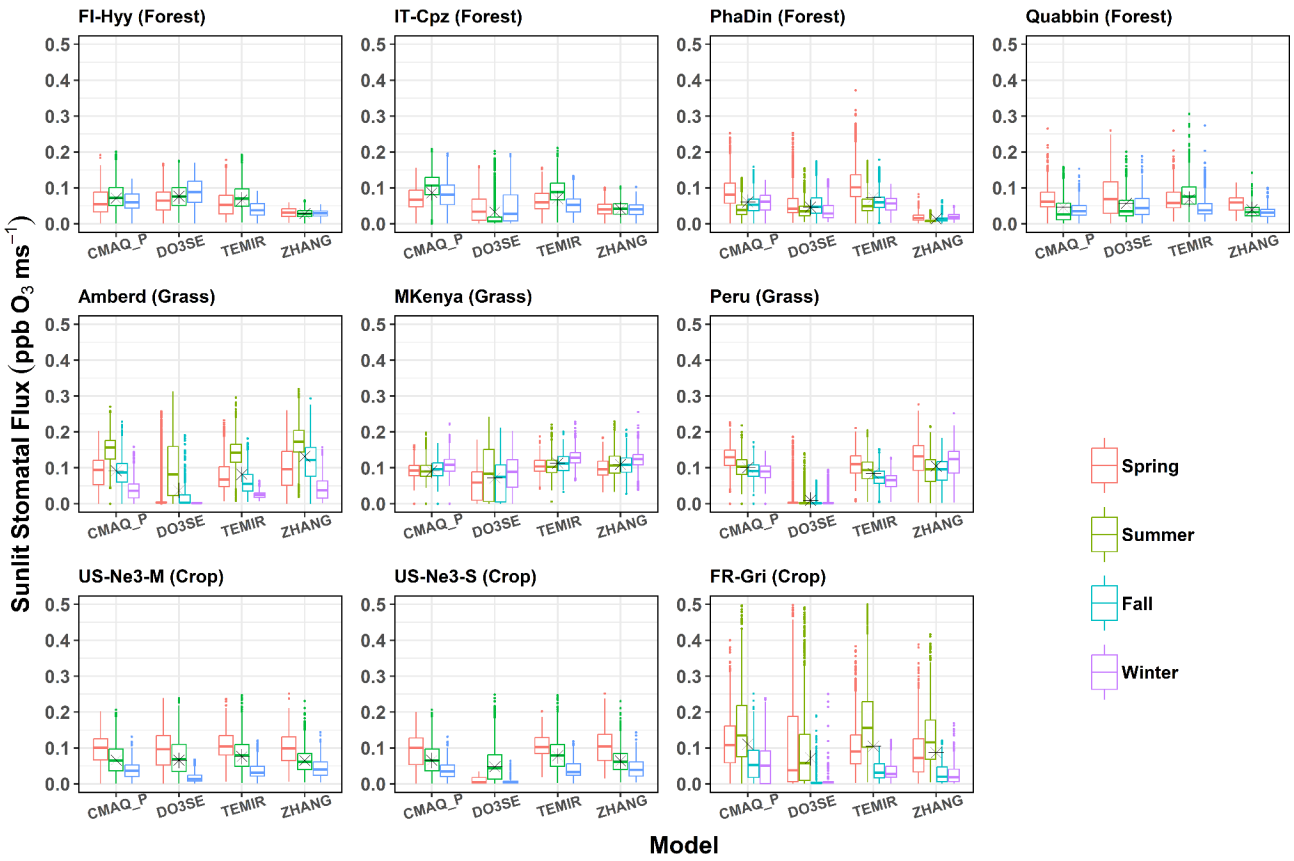

Figure 6. Box plots of seasonal mean leaf-level sunlit stomatal O_3 flux (ppb O_3 m s^{-1}) for different models across various sites (data represent SRAD > 50 W m^{-2} and the growing period). Asterisks indicate the annual mean flux.

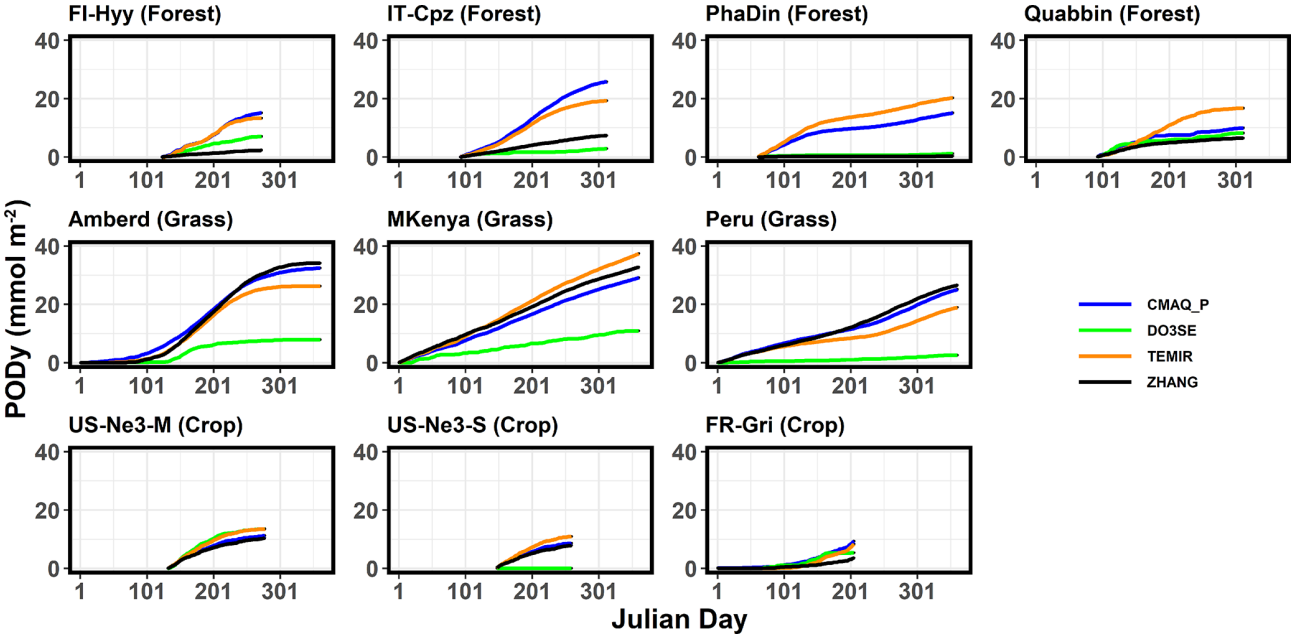

Figure 7. Evolution of POD_y (mmol O_3 m^{-2}) through the growing seasons at various sites.

sitivity was found at crops on average (2.7 mmol O_3 m^{-2}; 24.1 %), followed by grass (4.6 mmol O_3 m^{-2}; 17.2 %) and forest (1.6 mmol O_3 m^{-2}; 9.5 %). The responses unevenly vary in sign depending on the model because the temperature change depends on the optimal temperature at the specific sites: most models estimate a POD_y decrease when increasing temperature (Fig. 5). As described in Hayes et al. (2019), a temperature increase is seen in southern countries, where temperature could limit stomatal uptake since temperature is already close to the optimum in normal conditions. From our sensitivity analysis, temperature impacts on POD_y are noticeable only for a few sites (e.g. Ambered, Mt. Kenya, and Peru) and models' response to POD_y change were different due to different thresholds used for the temperature stress factors to stomatal conductance. The greatest changes in magnitude are predicted by Web-DO_3SE (5.1 mmol O_3 m^{-2}; 23.7 %), followed by CMAQ_P (3.1 mmol O_3 m^{-2}; 16.7 %), ZHANG (1.9 mmol O_3 m^{-2}; 14.1 %), and TEMIR (1.7 mmol O_3 m^{-2}; 9.6 %). In contrast, not all models are sensitive to changes of soil water content (SWC). The greatest response is seen in CMAQ_P (−6.3 and +1.4 mmol m^{-2}; −34.0 % and +7.6 %), followed by Web-DO_3SE (−2.2 and −2.2 mmol O_3 m^{-2}; −10.2 % and −10.2 %) and TEMIR (−1.1 and +0.8 mmol O_3 m^{-2}; −5.9 % and +4.3 %), while ZHANG shows no difference in this regard because it is not sensitive to soil moisture. The changes are largest at crops (1.5 mmol O_3 m^{-2}; 13.4 %), while grass and forest show similar responses (2.8 and 1.7 mmol O_3 m^{-2}; 10.5 % and 10.1 %, respectively). That is in line with De Marco et al. (2020), who show that POD_y responses to soil water changes increase with higher y threshold (here crops). The models do not appear to be sensitive to LAI 14 d shifts, with the only exception of Web-DO_3SE, which simulates a lower POD_y for both early and late LAI shifts (−2.6 mmol O_3 m^{-2} on average, across all land covers). LAI is used as a proxy for growing seasons in most models, whereas Web-DO_3SE considers growing seasons directly.

A 20 % change of $g_{max}/V_{c_{max}}$ leads to corresponding changes in POD_y values. An increase or decrease in the parameter leads to very similar changes (in ±) (Fig. 9, corresponding data in Tables S12–S14). The response appears to be generally uniform across sites. On average, the results show $+28.9 \pm 22.4$ % POD_y change for the 20 % increase in $g_{max}/V_{c_{max}}$ and -27.4 ± 13.1 % for the 20 % decrease with the largest absolute changes in grassland (up to 8 mmol O_3 m^{-2}, ZHANG). At forests and crops, changes up to 5 and 3 mmol O_3 m^{-2} occur, respectively. Among all sites, noticeably higher (the highest) relative changes were estimated at FR-Gri, which thus constituted the only relevant source of variability. This change is significantly different to the change at US-Ne3 (20 %–30 %) which reflects the contrasting low O_3 level at US-Ne3 compared to the highly polluted FR-Gri site. Also, the ZHANG model predicts the highest changes at crops while CMAQ_P seems insensitive. The ZHANG (and TEMIR) model appears to be the most sensitive model to the changes at most sites due to the strong dependency on the $g_{max}/V_{c_{max}}$ parameter (see analysis above). The only climate trend of the response is seen by the ZHANG model, which shows an average 65 % increase/decrease in wet forests (PhaDin, FI-Hyy) and only a 40 % change in dry places. Sites with very low estimates (PhaDin in ZHANG, Peru in Web-DO_3SE) were excluded from this sensitivity study.

To indicate the likely damage and range of damage that our modelled values of POD_y predict, we have used POD_y flux–response relationships available in the literature that most closely represent the vegetation type and climatic location of each study site (Table 5). To estimate O_3 damage to forests we use recently derived flux–response relationships that relate POD_1 values to gross annual increment (Karlsson et al., 2025) and hence indicate the annual change in growth rate caused by O_3. The mean model ensemble estimates a percentage reduction in gross annual increment of around 5 % for FI-Hyy and Pha Din, 6 % for IT-Cpz and 14 % for Quabbin. However, the range in estimates across models is not insignificant and most extreme at the Quabbin site, with a minimum of 11 % and a maximum of 21 % around the mean 13 % value; this is due to broadleaf deciduous species being more sensitive to the O_3 dose than needleleaf species and hence more sensitive to a range of POD_y model simulations (Bücker et al., 2015). It should also be emphasized that the Pha Din site uses a European-derived flux–response relationship for an Asian forest site.

For crops, flux–response relationships are available for wheat, maize, and soybeans (UNECE LRTAP, 2917; Peng et al., 2019; Zhang et al., 2017). These relationships are derived from Europe (wheat) and China (maize and soybean). For wheat, we see a large range in percentage yield loss, with a mean model ensemble of 26 % but a maximum yield loss of 35 %. This is driven by high POD_6 values derived from CMAQ_P and TEMIR. For maize at US-Ne3 the results are very consistent, with relative grain yield loss estimates ranging from 1.4 % to 1.6 %. For soybeans at US-Ne3, the results are less consistent than maize, with a minimum and maximum of 0 % and 35 % yield around a mean of 26 %. It is important to note that a Chinese-derived flux–response relationship is used to estimate O_3 damage on both US-grown crops.

Finally, for grasslands, we estimate total biomass losses of 19 %, 24 %, and 23 % from the ensemble model mean for Peru, Mt. Kenya, and Amberd respectively. The range in model values is relatively small for Amberd and Mt. Kenya. A low minimum value of 6 % total biomass loss is estimated for Peru due to the Web-DO_3SE model having a very low POD_y at this location due to a likely oversensitive limitation to O_3 uptake caused by low temperatures.

Table 5. Estimates of O_3 damage (for specific response metrics) derived from using the ensemble mean modelled POD_y values (and minimum and maximum values) with appropriate flux–response relationships based on land cover type. The climatic locations within which the flux–response relationships are derived are stated to show the relevance of their use in estimating damage. Shaded cells denote flux–response relationships that are derived outside of the broad climate region to which they are applied in this study and hence whose damage estimates should be treated with caution.

Site	Species	y	Flux–response relationship	Response metric & species	POD_y			% Response			Location of POD_y relationship	Reference
					min	median	max	min	median	max		
FI-Hyy	Scots pine	1	$y = -0.0057x + 1.0015$	gross annual increment (GAI) % for Norway spruce/Scots pine	2.3	10.2	15.1	1.2	5.6	8.5	Europe	Karlsson et al. (2025)
Quabbin	Birch/beech (broadleaf deciduous)	1	$y = -0.0093x + 0.9461$	gross annual increment (GAI) % for birch/beech	6.5	9.1	16.8	11.4	13.9	21.0	Europe	Karlsson et al. (2025)
PhaDin	Norway spruce (evergreen needleleaf)	1	$y = -0.0057x + 1.0015$	gross annual increment (GAI) % for Norway spruce/Scots pine	0.4	8.1	20.3	0.0	4.5	11.4	Europe	Karlsson et al. (2025)
IT-Cpz	Holm oak	1	$y = -0.0047x + 1.001$	gross annual increment (GAI) % for Aleppo pine/holm oak	2.8	13.3	25.8	1.2	6.2	12.0	Europe	Karlsson et al. (2025)
FR-Gri	Winter wheat	6	$y = -0.0385x + 1.003$	% grain yield loss for wheat	3.6	6.8	9.3	13.6	25.9	35.5	Europe	UNECE LRTAP (2017)
US-Ne3 (Maize)	Maize	6	$y = 0.0426x + 1$	% grain yield loss for wheat	10.5	12.4	13.6					Peng et al. (2019)
US-Ne3 (Soybean)	Soybean	6	$y = -0.033x + 1.01$	% relative seed yield loss per soybean plant	0.0	8.3	11.0	0.0	26.4	35.3	China	Zhang et al. (2017)
Amberd	Grassland	1	$y = -0.0062x + 0.947$	% total biomass loss for temperate perennial grassland	7.9	29.4	34.1	10.2	23.5	26.4	Europe	UNECE LRTAP (2017)
MKenya	Grassland	1	$y = -0.0062x + 0.947$	% total biomass loss for temperate perennial grassland	10.9	31.0	37.4	12.1	24.5	28.5	Europe	UNECE LRTAP(2017)
Peru	Grassland	1	$y = -0.0062x + 0.947$	% total biomass loss for temperate perennial grassland	2.6	22.1	26.6	6.9	19.0	21.8	Europe	UNECE LRTAP (2017)

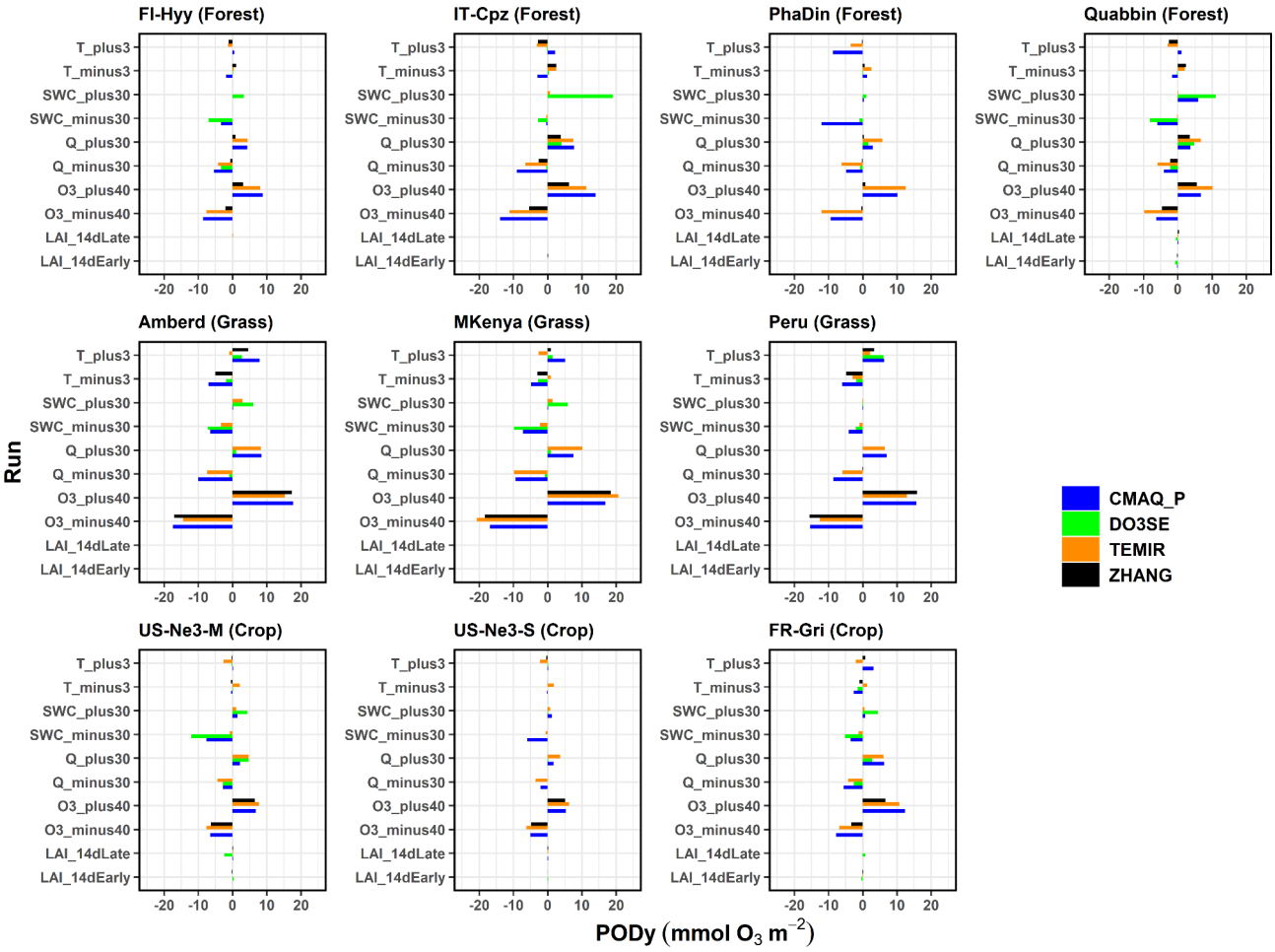

Figure 8. Meteorology sensitivity assessment: absolute change of POD_y values with respect to base run POD_y due to 10 % or 20 % variation of the temperature (T), soil water content (SWC), absolute humidity (Q), O_3, and LAI/growing season.

4 Discussion and conclusion

Here we have compared six deposition schemes commonly used in atmospheric chemistry transport models. We have focussed on the stomatal component of deposition since this is acknowledged to have a substantial influence on damage to vegetation and ultimately the ability of these six models to estimate the POD_y metric designed to indicate the level of O_3 damage to forest, crops, and grasslands. The models estimate POD_y values of 28, 15, and 9 mmol O_3 m^{-2} for grassland, forests, and crops, respectively. The multi-model mean estimates are generally in the expected range, which suggests that the stomatal flux output of these models could be used for O_3 impact assessments. We also explored the differences in POD_y by geographical location. When comparing one vegetation type, we find multiple drivers including O_3 concentration. The different model types are not the driving force; instead, the models can predict similar results.

There are three key reasons for differences in dry deposition model estimates: (i) model construct and the inclusion/exclusion of important factors that determine G_{st} and G_{sun}; (ii) model parameterization, which may characterize the land cover types; and (iii) differing model sensitivity to climate variables (seasonal, location effects) in estimates of stomatal deposition. The model comparison of stomatal conductance and stomatal dry deposition for ozone helps us to understand the differences between models. We found that models simulate generally reasonable stomatal deposition of 0.5–0.8 cm s^{-1} in summer, whereas the different model types often agree very well with each other. The stomatal conductance estimates among the models agree with correlation coefficients of 0.75, 0.80, and 0.85 for forests, crops, and grasslands. Thereby, the nine sites selected for this study also reflect different climate conditions; however the selection of sites that provide such broad representations also means that the analysis and the results cannot be generalized. The global coverage, diverse land types, and varying meteorological conditions of the nine sites resulted in widespread model responses to soil moisture (Fig. 8) while appearing to be insensitive to changes of LAI (Fig. 9). The former

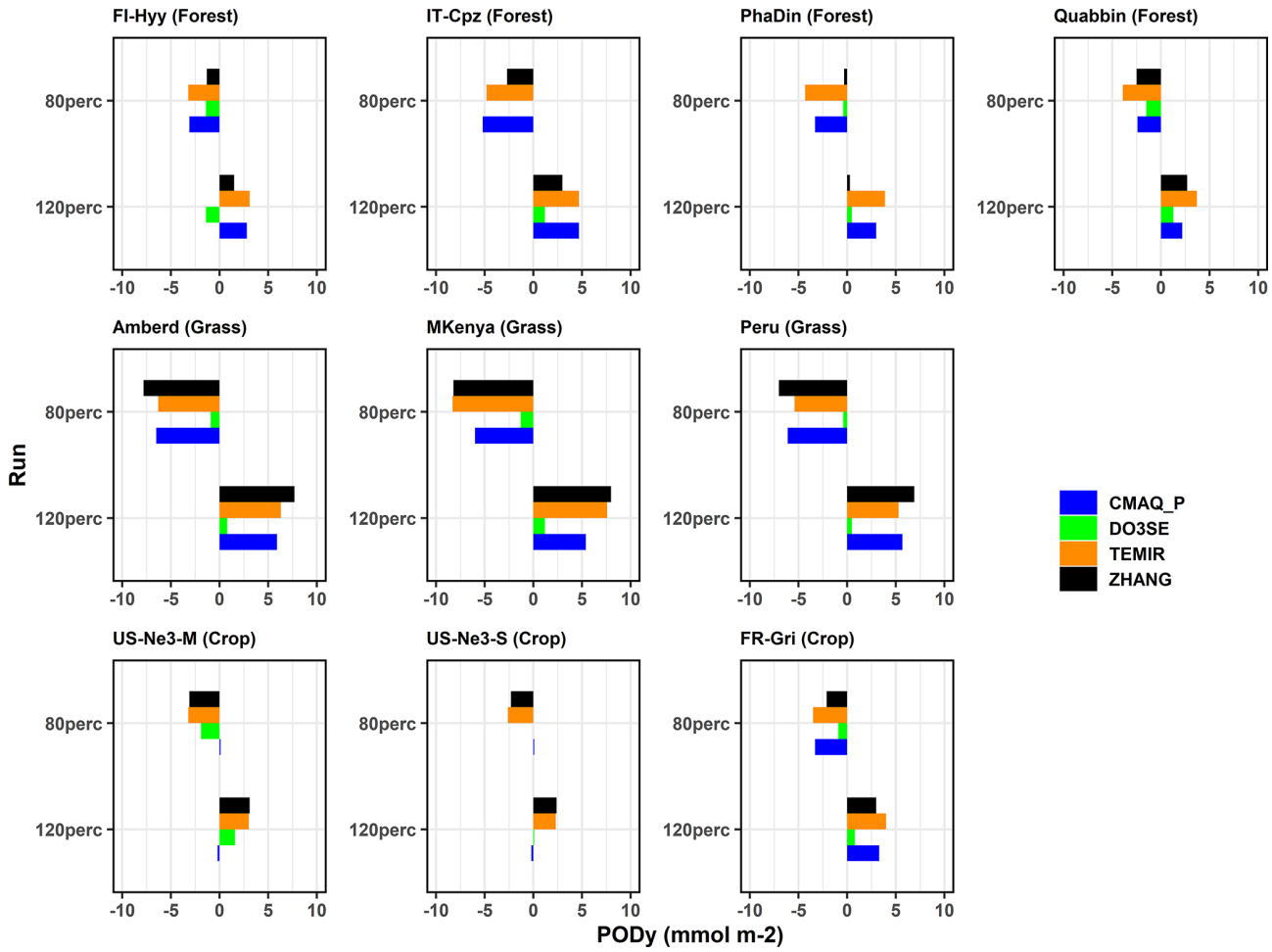

Figure 9. Land cover parameterization sensitivity assessment: absolute change of POD_y values with respect to the base run POD_y values due to 20 % variation of G_{max} or $V_{C_{max}}$.

underscored the idiosyncratic features and hence potential limitations of individual models, whereas the latter gave us confidence in model capabilities despite the different constructs and parameterizations of the models. The model differences, identified during this analysis, can be explained by the model's dependence on the meteorological conditions at sites. Indeed, both model structure (e.g. Raghav et al., 2023) and parameters (Fares et al., 2013) can affect the accuracy of stomatal conductance models. However, studies have shown that when properly calibrated against field observations, structurally different stomatal models can produce similar stomatal conductance (Fares et al., 2013; Mäkelä et al., 2019). Calibrating the key parameters of stomatal conductance models (e.g. $g_{max}/V_{c_{max}}$) is a crucial next step to improve the accuracy of stomatal conductance and POD_y estimates, as our sensitivity tests show a direct and possible non-linear relationship between POD_y and $g_{max}/V_{c_{max}}$ (e.g. at FR-Gri). This is possible with the recent availability of standardized global eddy flux (FLUXNET, Pastorello et al., 2020) and sap flow (SAPFLUXNET, Poyatos et al., 2021) data.

To estimate POD_y for a representative leaf of the upper canopy, the sunlit leaf must be distinguished from the total leaf. Since the effects-based community recognized that sunlit leaves contribute most to carbon assimilation throughout the growing season or O_3-sensitive period (e.g. in wheat, this is considered to be the time from anthesis to maturity), it will better represent damaging O_3 uptake. All flux–response relationships for POD_y are developed for such a representative leaf. This is an important distinction since previous model comparison studies (e.g. Clifton et al., 2023) have tended to focus on whole canopy dynamics. These are important to estimate accurately, but estimating POD_y requires additional canopy-level processes, which need (i) O_3 concentration at the top of the canopy, (ii) wind speed at the top of the canopy, and (iii) G_{sun} of a representative leaf at the top of the canopy. Studies (Emberson, 2020, and references therein) have established thresholds for different land cover types, which are used to provide y values for the selected sites with specific

land cover types in this study. Some studies suggest that the y threshold for land cover types may vary by global region (e.g. a number of studies suggest higher y values of up to 12 nmol O_3 m^2 s^{-1} are more appropriate for crops and forest tree species in Asia). In this study, which focuses on comparing across models, we maintain consistency and use common y threshold values for each land cover type. However, this is an aspect that would benefit from further study in the future since estimating POD_y values with higher thresholds is more challenging for all types of model given the less frequent occurrences of such high O_3 doses.

Our models estimate 30 %–50 % of stomatal O_3 deposition at sunlit leaves. Thereby, the model estimates of the total stomatal flux are more widespread (during one season) than the estimates of the sunlit only, which suggests an important role of the model's partitioning in two big leaves. When calculating POD_y model means, estimates generally agree with the literature, but most discrepancies between model estimates of POD_y ultimately come down to the differences in simulations of stomatal conductance. The sensitivity analysis of POD_y yields ozone as the most important input variable, to whose changes all models respond similarly. Considering all models and sites together, POD_y was affected most by the O_3 concentration (±60 %–80 % site-dependent; i.e. higher O_3 concentration leads to higher POD_y), followed by humidity (30 %–50 % site-dependent impact). Soil moisture impacts were also significant for the CMAQ_P and WebDO$_3$SE model (up to ±68 % and 22 % change). The sensitivity to temperature changes varies strongly among the model and its parameterization. As the plant canopy acts as a persistent sink of O_3, there is a significant vertical gradient of O_3 within the atmospheric surface layer. For example, Travis and Jacob (2019) show that the midday O_3 concentration at 65 m above ground (mid-point of a first vertical layer of GEOS-Chem v9-02) is 3 ppb higher than the O_3 concentration at 10 m above ground (inferred by Monin–Obukhov similarity theory, MOST) over the Southeastern United States. A mismatch between O_3 measurement height and canopy height can lead to inaccurate POD_y calculation (Gerosa et al., 2017). An O_3 bias of 2 ppb as estimated by, for example, Tarasick et al. (2019) would lead to a change of 6 %–7 % in POD1 (Gerosa et al., 2017). Similarly, we show that the errors in O_3 concentrations propagate non-linearly to POD_y (i.e. 40 % changes in O_3 leads to 53 %–68 % changes in POD_y); such a mismatch should be carefully avoided by applying atmospheric surface layer theories (e.g. MOST) to estimate the vertical profile of O_3, and therefore the canopy-top O_3 concentration, if direct measurement or model output of O_3 at canopy top is not available.

Finally, we use flux–response relationships for temperate deciduous (beech/birch), temperate needleleaf (Norway spruce (*Picea abies*)), crops (wheat (*Triticum aestivum*), maize (*Zea mays*), soybeans (*Glycine max*)), and grassland (*Lolium perenne*) to suggest the potential likely variation of damage estimates by land cover type and climatic region. These relationships have predominantly been developed for European and Asia forest and crop species. Therefore, they should be applied to other climate regions with caution, although recent evidence suggests that tropical forest species may have similar sensitivity to O_3 as European species (Cheeseman et al., 2024). Although there is rather large variability in POD_y values estimated by the model, the median values are relatively robust. Unfortunately, there is only statistical or modelled evidence of actual O_3 damage and only at a few of the sites investigated. Modelled evidence uses stomatal ozone flux models similar to those used in this study but which have been parameterized for local site conditions (Stella et al., 2013, for FR-Gri wheat). Simulations with a terrestrial biosphere model suggested an average long-term O_3 inhibition of 10.4 % for the period 1992–2011 at the Harvard site (Yue et al., 2016); this compares to our model ensemble estimate of 14 % GAI biomass loss for Quabbin. A significant but small NEP reduction was found during spring in the Italian Castelporziano forest site (up to −1.37 %) but not at the FI-Hyy or FR-Gri sites (Savi et al., 2020). Our modelling estimated substantially lower POD_y values and associated damage at Hyy and IT-Cpz than Quabbin, though we would expect to see a more substantial O_3 effect than that demonstrated by the NEP statistical modelling (i.e. 5 % and 6 % GAI biomass loss at FI-Hyy and IT-Cpz respectively). Similar simulations with a different terrestrial biosphere model found only moderate O_3 damage effects (GPP reductions of 4 %–6 %; Yue and Unger, 2014). This result is driven by low ambient ozone concentrations but also by the choice of a C_4 photosynthetic mechanism to estimate stomatal conductance which gives relatively high water use efficiency). These simulations also suggested that the US-Ne3 experienced a higher ozone effect on GPP than Harvard, which is consistent with our modelling for soybeans (but not maize, generally considered an O_3-tolerant crop species; Mills et al., 2011). According to the POD_6 estimates made using a SURFATM model, parameterized for Grignon wheat, POD_6 values of 1.094 mmol O_3 m^{-2} were estimated from 1 April to 1 July 2009, which compared with our range of 3.6 to 9.3; the locally parameterized values gave estimated crop yield losses of 4.2 %, compared to our median model ensemble estimates of 25 % for the winter wheat. This is most likely due to the lower g_{max} value used in the local parameterization (296 mmol O_3 m^{-2} s^{-1}). However, no recording of actual damage is given at the FR-Gri site, so it is not possible to tell which of these simulated damage estimates is closer to reality.

The experiments performed here with varying climate and vegetation input data also find a similar sensitivity of POD_y to O_3. It is helpful to have a range of models and model constructs in deposition schemes, especially where these have been developed for particular land cover types. When used in damage estimates it is important to ensure that key stressors are included, which may be important for that respective geographical region (such as soil and vapour pressure

deficit). Recognizing that several deposition schemes would be able to reliably predict POD_y for different climates and cover types once they have been parameterized appropriately will extend the usefulness of flux–response relationships.

Overall, this study has demonstrated the widespread applicability and consensus among various numerical stomatal flux methods. Both semi-mechanistic and empirical models can generally represent observed ozone fluxes among different land cover types and climates. We identified the key model constructs and parameterizations that cause differences in POD_y estimates. However, none of the models clearly shows a superior overall performance. Instead, all models can be effectively applied, each with its own strengths and weaknesses. Our findings present exciting opportunities to extend applications beyond specific sites and growing seasons, enabling comprehensive global stomatal flux studies over longer periods. Integrating the TOAR database with the Web-DO_3SE model enables automatic model runs for ozone–vegetation impact assessment at a large range of sites using the TOAR database.

Appendix A: Abbreviations

rsmin	Minimum stomatal resistance [$s\,m^{-1}$]
g_{smax}	Maximum stomatal conductance [$m\,s^{-1}$]
RH	Relative humidity [%]
LAI	Leaf area index [$m^2\,m^{-2}$]
sd, sn	Snow depth [m] and snow cover
ssrd, strd	Solar and thermal flux at surface [$W\,m^{-2}$]
sw	Soil wetness [m]
al_vis:	Albedo (visible)
cwv	Canopy water content [$kg\,m^{-2}$]
SWC	Soil water content
SM	Soil moisture [$m^3\,m^{-3}$]
wdir	Wind direction [°]
wspeed	Wind speed [$m\,s^{-1}$]
cv	Vegetation fraction [$m^2\,m^{-2}$]
P	Precipitation [mm]
P_rate	Precipitation rate [$mm\,h^{-1}$], [$kg\,m^{-2}\,s^{-1}$], [$m\,s^{-1}$]
T_{air}, T_{soil}, T2m	Air, soil, 2 m temperature in [K]
VPD	Vapour pressure deficit [kPa]
Pa	Air pressure [hPa]
R_n, G_r	Net and global radiation [$W\,m^{-2}$]
$u*$	Friction velocity [$m\,s^{-1}$]
O_3, CO_2	O_3 and CO_2 concentration [ppb], [ppt]
h_dis, z0	Displacement height [m], roughness length [m]
CF	Cloud fraction
LUC	Land use category

Code availability. The Web-DO_3SE source code is freely available at https://toar-data.fz-juelich.de/ (last access: 1 September 2025) under the CC-BY 4.0 license (https://creativecommons.org/licenses/by/4.0/, last access: 21 September 2024). The further model code can be obtained upon request.

Data availability. The TOAR data are freely available at https://doi.org/10.34730/4d9a287dec0b42f1aa6d244de8f19eb3 (Schröder et al. 2021) under the CC-BY 4.0 license (https://creativecommons.org/licenses/by/4.0/, last access: 21 September 2024). The ERA5 data used can be downloaded from the MeteoCloud server (Forschungszentrum Jülich, 2024). The FLUXNET 2015 dataset is publicly available at https://fluxnet.org/data/fluxnet2015-dataset/ (last access: 21 August 2024). Stomatal conductance estimates, and the related FLUXNET 2015 data from SynFlux version 2, can be obtained by contacting Christopher Holmes. The model outputs are available from Zenodo (https://doi.org/10.5281/zenodo.15812487; Emmerichs, 2025).

Supplement. The supplement related to this article is available online at https://doi.org/10.5194/bg-22-4823-2025-supplement.

Author contributions. TE: site selection, TOAR data extraction, data preparation, model support, modelling Web-DO_3SE, writing, and coordination. AAM: modelling (ZHANG, MESSy, NOAH-GEM, TEMIR model), statistics, plots, and analysis. LE: concept and writing. HM: writing and reviewing. LZ: concept and writing. LR: modelling with CMAQ and FLUXNET data preparation. CB: debugging and test simulations of Web-DO3SE. AW: site selection and preparation of FLUXNET and sensitivity data. GK: site selection and TOAR data extraction. GG: site analysis. MH: plots and reviewing. PG: POD_y analysis.

Competing interests. The contact author has declared that none of the authors has any competing interests.

Disclaimer. Publisher's note: Copernicus Publications remains neutral with regard to jurisdictional claims made in the text, published maps, institutional affiliations, or any other geographical representation in this paper. While Copernicus Publications makes every effort to include appropriate place names, the final responsibility lies with the authors.

Acknowledgements. We acknowledge the TOAR team supporting the data extraction. The authors acknowledge the access to the meteorological data on the Jülich MeteoCloud provided by Jülich Supercomputing Centre (Krause and Thörnig, 2018). Tamara Emmerichs thanks the German Research Foundation as part of the CLICCS Clusters of Excellence (DFG EXC 2037). We thank the responsible people of the selected measurement sites for their support in obtaining site information. We greatly appreciate helpful discussions

in the earlier stages of the project from the following people: Owen Cooper, Zhaozhong Feng, Laurens Ganzeveld, Meiyun Lin, Martin Schultz, Eran Tas, and Oliver Wild.

Financial support. The article processing charges for this open-access publication were covered by the Forschungszentrum Jülich.

Review statement. This paper was edited by Ivonne Trebs and reviewed by two anonymous referees.

References

Ainsworth, E. A.: Understanding and improving global crop response to ozone pollution, The Plant Journal, 90, 886–897, https://doi.org/10.1111/tpj.13298, 2017.

Ainsworth, E. A., Yendrek, C. R., Sitch, S., Collins, W. J., and Emberson, L. D.: The effects of tropospheric ozone on net primary productivity and implications for climate change, Annu. Rev. plant Biol., 63, 637–661, https://doi.org/10.1146/annurev-arplant-042110-103829, 2012.

Amos, B., Arkebauer, T. J., and Doran, J. W.: Soil surface fluxes of greenhouse gases in an irrigated maize-based agroecosystem, Soil Sci. Soc. Am. J., 69, 387–395, https://doi.org/10.2136/sssaj2005.0387, 2005.

Avnery, S., Mauzerall, D. L., Liu, J., and Horowitz, L. W.: Global Crop Yield Reductions due to Surface Ozone Exposure: 1. Year 2000 Crop Production Losses and Economic Damage, Atmos. Environ., 45, 2284–2296, https://doi.org/10.1016/j.atmosenv.2010.11.045, 2011.

Ball, J. T., Woodrow, I. E., and Berry, J. A.: A Model Predicting Stomatal Conductance and its Contribution to the Control of Photosynthesis under Different Environmental Conditions. in: Progress in Photosynthesis Research, edited by: Biggins, J., Springer, Dordrecht, https://doi.org/10.1007/978-94-017-0519-6_48, 1987.

Beck, H. E., McVicar, T. R., Vergopolan, N. Berg, A., Lutsko, N. J., Dufour, A., Zeng, Z., Jiang, X., van Dijk, A. I. J. M., and Miralles, D. G.: High-resolution (1 km) Köppen-Geiger maps for 1901–2099 based on constrained CMIP6 projections, Sci. Data, 10, 724, https://doi.org/10.1038/s41597-023-02549-6, 2023.

Büker, P., Feng, Z., Uddling, J., Briolat, A., Alonso, R., Braun, S., Elvira, S., Gerosa, G., Karlsson, P. E., Le Thiec, D., and Marzuoli, R.: New flux based dose–response relationships for ozone for European forest tree species, Environ. Pollut., 206, 163–174, https://doi.org/10.1016/j.envpol.2015.06.033, 2015.

Bukowiecki, N., Steinbacher, M., Henne, S., Nguyen, N. A., Nguyen, X. A., Hoang, A. L., Nguyen, D. L., Duong, H. L., Engling, G., Wehrle, G., Gysel-Beer, M., and Baltensperger, U.: Effect of Large-scale Biomass Burning on Aerosol Optical Properties at the GAW Regional Station Pha Din, Vietnam, Aerosol Air Qual. Res., 19, 1172–1187, https://doi.org/10.4209/aaqr.2018.11.0406, 2018.

Cheesman, A. W., Brown, F., Artaxo, P., Farha, M. F., Folberth, G. A., Hayes, F. A., Viola, V. H. A., Hill, T. C., Mercado, L. M., Oliver, R. J., O'Sullivan, M., Udling, J., Cernusak, L. A., and Sitch, S.: Reduced productivity and carbon drawdown of tropical forests from ground-level ozone exposure, Nat. Geosci. 17, 1003–1007, https://doi.org/10.1038/s41561-024-01530-1, 2024.

Chen, X., Quéléver, L. L. J., Fung, P. L., Kesti, J., Rissanen, M. P., Bäck, J., Keronen, P., Junninen, H., Petäjä, T., Kerminen, V.-M., and Kulmala, M.: Observations of ozone depletion events in a Finnish boreal forest, Atmos. Chem. Phys., 18, 49–63, https://doi.org/10.5194/acp-18-49-2018, 2018.

Clifton, O. E., Fiore, A. M., Munger, J. W., and Wehr, R.: Spatiotemporal controls on observed daytime ozone deposition velocity over northeastern US forests during summer, J. Geophys. Res.-Atmos., 124, 5612–5628, https://doi.org/10.1029/2018JD029073, 2019.

Clifton, O. E., Lombardozzi, D. L., Fiore, A. M., Paulot, F., and Horowitz, L. W.: Stomatal conductance influences interannual variability and long-term changes in regional cumulative plant uptake of ozone, Environ. Res. Lett., 15, 114059, https://doi.org/10.1088/1748-9326/abc3f1, 2020a.

Clifton, O. E., Paulot, F., Fiore, A. M., Horowitz, L. W., Correa, G., Baublitz, C. B., Fares, S., Goded, I., Goldstein, A. H., Gruening, C., Hogg, A. J., Loubet, B., Mammarella, I., Munger, J. W., Neil, L., Stella, P., Uddling, J., Vesala, T., and Weng, E.: Influence of dynamic ozone dry deposition on ozone pollution, J. Geophys. Res.-Atmos., 125, e2020JD032398, https://doi.org/10.1029/2020JD032398, 2020b.

Clifton, O. E., Schwede, D., Hogrefe, C., Bash, J. O., Bland, S., Cheung, P., Coyle, M., Emberson, L., Flemming, J., Fredj, E., Galmarini, S., Ganzeveld, L., Gazetas, O., Goded, I., Holmes, C. D., Horváth, L., Huijnen, V., Li, Q., Makar, P. A., Mammarella, I., Manca, G., Munger, J. W., Pérez-Camanyo, J. L., Pleim, J., Ran, L., San Jose, R., Silva, S. J., Staebler, R., Sun, S., Tai, A. P. K., Tas, E., Vesala, T., Weidinger, T., Wu, Z., and Zhang, L.: A single-point modeling approach for the intercomparison and evaluation of ozone dry deposition across chemical transport models (Activity 2 of AQMEII4), Atmos. Chem. Phys., 23, 9911–9961, https://doi.org/10.5194/acp-23-9911-2023, 2023.

Collatz, G. J., Ball, J. T., Grivet, C., and Berry, J. A.: Physiological and environmental regulation of stomatal conductance, photosynthesis and transpiration: a model that includes a laminar boundary layer, Agricultural and Forest Meteorology, https://doi.org/10.1016/0168-1923(91)90002-8, 1991.

Copernicus Climate Change Service (C3S): ERA5: Fifth generation of ECMWF atmospheric reanalyses of the global climate, Copernicus Climate Change Service Climate Data Store (CDS) [data set], https://cds.climate.copernicus.eu/datasets/reanalysis-era5-complete?tab=d_download (last access: 27 November 2024), 2017.

De Marco, A., Anav, A., Sicard, P., Feng, Z., and Paoletti, E.: High spatial resolution ozone risk-assessment for Asian forests, Environ. Res. Lett., 15, 104095, https://doi.org/10.1088/1748-9326/abb501, 2020.

Ducker, J. A., Holmes, C. D., Keenan, T. F., Fares, S., Goldstein, A. H., Mammarella, I., Munger, J. W., and Schnell, J.: Synthetic ozone deposition and stomatal uptake at flux tower sites, Biogeosciences, 15, 5395–5413, https://doi.org/10.5194/bg-15-5395-2018, 2018.

Emberson, L. D., Ashmore, M. R., Cambridge, H. M., Simpson, D., and Tuovinen, J. P.: Modelling stomatal ozone flux across Europe, Environmental Pollution, 109, 403–413, https://doi.org/10.1016/S0269-7491(00)00043-9, 2000.

Emberson, L.: Effects of ozone on agriculture, forests and grasslands, Philos. T. Roy. Soc. A, 378, 20190327, https://doi.org/10.1098/rsta.2019.0327, 2020.

Emmerichs, T.: Model outputs from the study "Can atmospheric chemistry deposition schemes reliably simulate stomatal ozone flux across global land covers and climates?", Zenodo [data set], https://doi.org/10.5281/zenodo.15812487, 2025.

Emmerichs, T., Kerkweg, A., Ouwersloot, H., Fares, S., Mammarella, I., and Taraborrelli, D.: A revised dry deposition scheme for land–atmosphere exchange of trace gases in ECHAM/MESSy v2.54, Geosci. Model Dev., 14, 495–519, https://doi.org/10.5194/gmd-14-495-2021, 2021.

Fares, S., Weber, R., Park, J. H., Gentner, D., Karlik, J., and Goldstein, A. H.: Ozone deposition to an orange orchard: Partitioning between stomatal and non-stomatal sinks, Environmental Pollution, 169, 258–266, https://doi.org/10.1016/j.envpol.2012.01.030, 2012.

Fares, S., Mereu, S., Scarascia Mugnozza, G., Vitale, M., Manes, F., Frattoni, M., Ciccioli, P., Gerosa, G., and Loreto, F.: The ACCENT-VOCBAS field campaign on biosphere-atmosphere interactions in a Mediterranean ecosystem of Castelporziano (Rome): site characteristics, climatic and meteorological conditions, and eco-physiology of vegetation, Biogeosciences, 6, 1043–1058, https://doi.org/10.5194/bg-6-1043-2009, 2009.

Fares, S., Matteucci, G., Scarascia Mugnozza, G., Morani, A., Calfapietra, C., Salvatori, E., L. Fusaro, L., Manes, F., and Loreto, F.: Testing of models of stomatal ozone fluxes with field measurements in a mixed Mediterranean forest, Atmos. Environ., 67, 242–251, https://doi.org/10.1016/j.atmosenv.2012.11.007, 2013.

Fares, S., Savi, F., Muller, J., Matteucci, G., and Paoletti, E.: Simultaneous measurements of above and below canopy ozone fluxes help partitioning ozone deposition between its various sinks in a Mediterranean Oak Forest, Agr. Forest Meteorol., 198, 181–191, https://doi.org/10.1016/j.agrformet.2014.08.014, 2014.

Farquhar, G.D., von Caemmerer, S., and Berry, J. A. A: biochemical model of photosynthetic CO2 assimilation in leaves of C3 species, Planta, 149, 78–90, https://doi.org/10.1007/BF00386231, 1980.

Feng, Z., Tang, H., Uddling, J., Pleijel, H., Kobayashi, K., Zhu, J., Oue, H., and Guo, W.: A stomatal ozone flux–response relationship to assess ozone-induced yield loss of winter wheat in subtropical China, Environ. Pollut., 164, 16–23, https://doi.org/10.1016/j.envpol.2012.01.014, 2012. Forschungszentrum Jülich: ECMWF reanalyses, Jülich meteocloud [data set], https://datapub.fz-juelich.de/slcs/meteocloud/doc_p_data1_slmet_met_data_ecmwf.html (last access: 15 July 2024), 2024.

Fuhrer, J., Val Martin, M., Mills, G., Heald, C. L., Harmens, H., Hayes, F., Sharp, K., Bender, J., and Ashmore, M. R.: Current and future ozone risks to global terrestrial biodiversity and ecosystem processes, Ecol. Evol., 6, 8785–8799, https://doi.org/10.1002/ece3.2568, 2016.

Ganzeveld, L. and Lelieveld, J.: Dry deposition parameterization in a chemistry general circulation model and its influence on the distribution of reactive trace gases, J. Geophys. Res.-Atmos., 100, 20999–21012, https://doi.org/10.1029/95JD02266, 1995.

Gerosa, G., Vitale, M., Finco, A., Manes, F., Denti, A. B., and Cieslik, S.: Ozone uptake by an evergreen Mediterranean Forest (Quercus ilex) in Italy. Part I: Micrometeorological flux measurements and flux partitioning, Atmos. Environ., 39, 3255–3266, https://doi.org/10.1016/j.atmosenv.2005.01.056, 2005.

Gerosa, G., Finco, A., Mereu, S., Vitale, M., Manes, F., and Denti, A. B.: Comparison of seasonal variations of ozone exposure and fluxes in a Mediterranean Holm oak forest between the exceptionally dry 2003 and the following year, Environmental Pollution, 157, 1737–1744, https://doi.org/10.1016/j.envpol.2007.11.025, 2009.

Gerosa, G., Marzuoli, R., Monteleone, B., Chiesa, M., and Finco, A.: Vertical ozone gradients above forests. Comparison of different calculation options with direct ozone measurements above a mature forest and consequences for ozone risk assessment, Forests, 8, 337, https://doi.org/10.3390/f8090337, 2017.

Goudriaan, J., van Laar, H. H., van Keulen, H., and Louwerse, W.: Photosynthesis, CO2 and Plant Production, in: Wheat Growth and Modelling, edited by: Day, W., and Atkin, R. K., NATO ASI Science, Springer, Boston, MA., vol 86., https://doi.org/10.1007/978-1-4899-3665-3_10, 1985.

Grulke, N. E. and Heath, R. L.: Ozone effects on plants in natural ecosystems, Plant Biol., 22, 12–37, https://doi.org/10.1111/plb.12971, 2020.

Guaita, P. R., Marzuoli, R., and Gerosa, G. A.: A regional scale flux-based O_3 risk assessment for winter wheat in northern Italy, and effects of different spatio-temporal resolutions, Environ. Pollut., 333, 121860, https://doi.org/10.1016/j.envpol.2023.121860, 2023.

Hardacre, C., Wild, O., and Emberson, L.: An evaluation of ozone dry deposition in global scale chemistry climate models, Atmos. Chem. Phys., 15, 6419–6436, https://doi.org/10.5194/acp-15-6419-2015, 2015.

Hayes, F., Mills, G., Harmens, H., and Norris, D.: Evidence of widespread ozone damage to vegetation in Europe (1990–2006), ICP Vegetation Programme Coordination Centre, CEH Bangor, UK, https://nora.nerc.ac.uk/id/eprint/1334/1/Evidence_Report_FINAL_PRINTED_VERSION_low-res.pdf (last access: 1 September 2025), 2007.

Hayes, F., Mills, G., Alonso, R., González-Fernández, I., Coyle, M., Grünhage, L., Gerosa, G., Karlsson, P. E., and Marzuoli, R.: A site-specific analysis of the implications of a changing ozone profile and climate for stomatal ozone fluxes in Europe, Water Air Soil Pollut., 230, 1–15, https://doi.org/10.1007/s11270-018-4057-x, 2019.

Henne, S., Junkermann, W., Kariuki, J. M., Aseyo, J., and Klausen, J.: Mount Kenya Global Atmosphere Watch Station (MKN): Installation and Meteorological Characterization, J. Appl. Meteor. Climatol., 47, 2946–2962, https://doi.org/10.1175/2008JAMC1834.1, 2008a.

Henne, S., Klausen, J., Junkermann, W., Kariuki, J. M., Aseyo, J. O., and Buchmann, B.: Representativeness and climatology of carbon monoxide and ozone at the global GAW station Mt. Kenya in equatorial Africa, Atmos. Chem. Phys., 8, 3119–3139, https://doi.org/10.5194/acp-8-3119-2008, 2008b.

Hersbach, H., Bell, B., Berrisford, P., Hirahara, S., Horányi, A., Muñoz-Sabater, J., Nicolas, J., Peubey, C., Radu, R., Schepers, D., Simmons, A., Soci, C., Abdalla, S., Abellan, X., Balsamo, G., Bechtold, P., Biavati, G., Bidlot, J., Bonavita, M., De Chiara, G., Dahlgren, P., Dee, D., Diamantakis, M., Dragani, R., Flemming, J., Forbes, R., Fuentes, M., Geer, A., Haimberger, L., Healy, S., Hogan, R. J., Hólm, E., Janisková, M., Keeley, S.,

Laloyaux, P., Lopez, P., Lupu, C., Radnoti, G., de Rosnay, P., Rozum, I., Vamborg, F., Villaume, S., and Thépaut, J.-N.: The ERA5 global reanalysis, Q. J. Roy. Meteor. Soc., 146, 1999–2049, https://doi.org/10.1002/qj.3803, 2020.

Horváth, L., Koncz, P., Móring, A., Nagy, Z., Pinter, K., and Weidinger, T.: An Attempt to Partition Stomatal and Non-stomatal Ozone Deposition Parts on a Short Grassland, Bound.-Lay. Meteorol., 167, 303–326, https://doi.org/10.1007/s10546-017-0310-x, 2018.

Huang, M., Crawford, J. H., Carmichael, G. R., Bowman, K. W., Kumar, S. V., and Sweeney, C.: Satellite soil moisture data assimilation impacts on modeling weather variables and ozone in the southeastern US – Part 2: Sensitivity to dry-deposition parameterizations, Atmos. Chem. Phys., 22, 7461–7487, https://doi.org/10.5194/acp-22-7461-2022, 2022.

Jägermeyr, J., Müller, C., Minoli, S., Ray, D., and Siebert, S.: GGCMI Phase 3 crop calendar, Zenodo [data set], https://doi.org/10.5281/zenodo.5062513, 2021a.

Jägermeyr, J., Müller, C., Ruane, A. C., Elliott, J., Balkovic, J., Castillo, O., Faye, B., Foster, I., Folberth, C., Franke, J. A., Fuchs, K., Guarin, J., Heinke, J., Hoogenboom, G., Iizumi, T., Kain, A. K., Kelly, D., Khabarov, N., Lange, S., Lin, T.-S., Liu, W., Mialyk, O., Minoli, S., Moyer, E. J., Okada, M., Phillips, M., Porter, C., Rabin, S., Scheer, C., Schneider, J. M., Schyns, J. F., Skalsky, R., Smerald, A., Stella, T., Stephens, H., Webber, H., Zabel, F., and Rosenzweig, C.: Climate impacts on global agriculture emerge earlier in new generation of climate and crop, Nature Food, 2, 873–885, https://doi.org/10.1038/s43016-021-00400-y, 2021b.

Jarvis, P.: The interpretation of the variations in leaf water potential and stomatal conductance found in canopies in the field, Philosophical Transactions of the Royal Society of London, B, Biological Sciences, 273, 593–610, https://doi.org/10.1098/rstb.1976.0035, 1976.

Junninen, H., Lauri, A., Keronen, P., Aalto, P., Hiltunen, V., Hari, P., and Kulmala, M.: Smart-SMEAR: online data exploration and visualization tool for SMEAR stations, Boreal Environ. Res., 14, 447–457, 2009.

Karlsson, P. E., Büker, P., Bland, S., Simpson, D., Sharps, K., Hayes, F., and Emberson, L. D.: Ozone causes substantial reductions in the carbon sequestration of managed European forests, Biogeosciences, 22, 3563–3582, https://doi.org/10.5194/bg-22-3563-2025, 2025.

Kattge, J. and Knorr, W.: Temperature acclimation in a biochemical model of photosynthesis: a reanalysis of data from 36 species, Plant Cell Environ., 30, 1176–1190, https://doi.org/10.1111/j.1365-3040.2007.01690.x, 2007.

Kerkweg, A., Buchholz, J., Ganzeveld, L., Pozzer, A., Tost, H., and Jöckel, P.: Technical Note: An implementation of the dry removal processes DRY DEPosition and SEDImentation in the Modular Earth Submodel System (MESSy), Atmos. Chem. Phys., 6, 4617–4632, https://doi.org/10.5194/acp-6-4617-2006, 2006.

Khan, A. M., Clifton, O. E., Bash, J. O., Bland, S., Booth, N., Cheung, P., Emberson, L., Flemming, J., Fredj, E., Galmarini, S., Ganzeveld, L., Gazetas, O., Goded, I., Hogrefe, C., Holmes, C. D., Horváth, L., Huijnen, V., Li, Q., Makar, P. A., Mammarella, I., Manca, G., Munger, J. W., Pérez-Camanyo, J. L., Pleim, J., Ran, L., San Jose, R., Schwede, D., Silva, S. J., Staebler, R., Sun, S., Tai, A. P. K., Tas, E., Vesala, T., Weidinger, T., Wu, Z., Zhang, L., and Stoy, P. C.: Ozone dry deposition through plant stomata: multi-model comparison with flux observations and the role of water stress as part of AQMEII4 Activity 2, Atmos. Chem. Phys., 25, 8613–8635, https://doi.org/10.5194/acp-25-8613-2025, 2025.

Krause, D. and Thörnig, P.: JURECA: modular supercomputer at Jülich supercomputing centre, Journal of large-scale research facilities JLSRF, 4, A132–A132, https://doi.org/10.17815/jlsrf-4-121-1, 2018.

Leuning, R.: Scaling to a common temperature improves the correlation between the photosynthesis parameters J max and V cmax, Journal of Experimental Botany, 48, 345–347, https://doi.org/10.1093/jxb/48.2.345, 1997.

Leung, F., Williams, K., Sitch, S., Tai, A. P. K., Wiltshire, A., Gornall, J., Ainsworth, E. A., Arkebauer, T., and Scoby, D.: Calibrating soybean parameters in JULES 5.0 from the US-Ne2/3 FLUXNET sites and the SoyFACE-O_3 experiment, Geosci. Model Dev., 13, 6201–6213, https://doi.org/10.5194/gmd-13-6201-2020, 2020.

Li, M., Wu, P., and Ma, Z.: A comprehensive evaluation of soil moisture and soil temperature from third-generation atmospheric and land reanalysis data sets, Int. J. Climatol, 40, 5744–5766, https://doi.org/10.1002/joc.6549, 2020.

Mao, H., Felker-Quinn, E., Sive, B., Zhang, L., Ye, Z., and Fang, H.: Examining indicators and methods for quantifying ozone exposure to vegetation, Atmospheric Environment, https://doi.org/10.1016/j.atmosenv.2023.120195, 2023.

Mäkelä, J., Knauer, J., Aurela, M., Black, A., Heimann, M., Kobayashi, H., Lohila, A., Mammarella, I., Margolis, H., Markkanen, T., Susiluoto, J., Thum, T., Viskari, T., Zaehle, S., and Aalto, T.: Parameter calibration and stomatal conductance formulation comparison for boreal forests with adaptive population importance sampler in the land surface model JSBACH, Geosci. Model Dev., 12, 4075–4098, https://doi.org/10.5194/gmd-12-4075-2019, 2019.

Mészáros, R., Horváth, L., Weidinger, T., Neftel, A., Nemitz, E., Dämmgen, U., Cellier, P., and Loubet, B.: Measurement and modelling ozone fluxes over a cut and fertilized grassland, Biogeosciences, 6, 1987–1999, https://doi.org/10.5194/bg-6-1987-2009, 2009.

Meyers, T. P., Finkelstein, P., Clarke, J., Ellestad, T. G., and Sims, P. F.: A multilayer model for inferring dry deposition using standard meteorological measurements, J. Geophys. Res.-Atmos., 103, 22645–22661, https://doi.org/10.1029/98JD01564, 1998.

Mills, G., Hayes, F., Simpson, D., Emberson, L., Norris, D., Harmens, H., and Büker, P.: Evidence of widespread effects of ozone on crops and (semi-)natural vegetation in Europe (1990–2006) in relation to AOT40- and flux-based risk maps, Glob. Change Biol., 17, 592–613, https://doi.org/10.1111/j.1365-2486.2010.02217.x, 2011.

Mills, G., Pleijel, H., Malley, C. S., Sinha, B., Cooper, O. R., Schultz, M. G., Neufeld, H. S., Simpson, D., Sharps, K., Feng, Z., Gerosa, G., Harmens, H., Kobayashi, K., Saxena, P., Paoletti, E., Sinha, V., and Xu, X.: Tropospheric Ozone Assessment Report: Present-day tropospheric ozone distribution and trends relevant to vegetation, Elementa, 6, 47, https://doi.org/10.1525/elementa.302, 2018.

Nelson, J. A., Carvalhais, N., Cuntz, M., Delpierre, N., Knauer, J., Ogée, J., Migliavacca, M., Reichstein, M.,

and Jung, M.: Coupling water and carbon fluxes to constrain estimates of transpiration: The TEA algorithm. Journal of Geophysical Research: Biogeosciences, 123, 3617–3632, https://doi.org/10.1029/2018JG004727, 2018.

Niyogi, D. S., Alapaty, K., Raman, S., and Chen, F.: Development and evaluation of a coupled Photosynthesis-Based Gas Exchange Evapotranspiration Model (GEM) for mesoscale weather forecasting applications, J. Appl. Meteorol. Climatol., 48(2), https://doi.org/10.1175/2008JAMC1662.1, 2009.

Oleson, K. W., Lawrence, D. M., Bonan, G. B., Drewniak, B., Huang, M., Koven, C. D., Levis, S., Li, F., Riley, W. J., Subin, Z. M., Swenson, S. C., and Thornton, P. E.: Technical Description of version 4.5 of the Community Land Model (CLM), NCAR Technical Note NCAR/TN-503+STR, National Center for Atmospheric Research, Boulder, CO, 422 pp., https://doi.org/10.5065/D6RR1W7M, 2013.

Pastorello, G., Trotta, C., and Canfora, E.: The FLUXNET2015 dataset and the ONEFlux processing pipeline for eddy covariance data, Sci Data, 7, 225, https://doi.org/10.1038/s41597-020-0534-3, 2020.

Peng, J., Shang, B., Xu, Y., Feng, Z., Pleijel, H., and Calatayud, V.: Ozone exposure-and flux-yield response relationships for maize, Environ. Pollut., 252, 1–7, 2019.

Pieber, S. M., Henne, S., Nguyen, N. A., Nguyen, D. L., and Steinbacher, M.: Trace Gases and Air Quality in Northwestern Vietnam During Recurrent Biomass Burning on the Indochina Peninsula Since 2014 – Field Observations and Atmospheric Simulations, in: Vegetation Fires and Pollution in Asia, edited by: Vadrevu, K. P., Ohara, T., and Justice, C.,Springer, Cham, https://doi.org/10.1007/978-3-031-29916-2_32, 2023.

Pleim, J. and Ran, L.: Surface flux modeling for air quality applications, Atmosphere, 2, 271–302, https://doi.org/10.3390/atmos2030271, 2011.

Poyatos, R., Granda, V., Flo, V., Adams, M. A., Adorján, B., Aguadé, D., Aidar, M. P. M., Allen, S., Alvarado-Barrientos, M. S., Anderson-Teixeira, K. J., Aparecido, L. M., Arain, M. A., Aranda, I., Asbjornsen, H., Baxter, R., Beamesderfer, E., Berry, Z. C., Berveiller, D., Blakely, B., Boggs, J., Bohrer, G., Bolstad, P. V., Bonal, D., Bracho, R., Brito, P., Brodeur, J., Casanoves, F., Chave, J., Chen, H., Cisneros, C., Clark, K., Cremonese, E., Dang, H., David, J. S., David, T. S., Delpierre, N., Desai, A. R., Do, F. C., Dohnal, M., Domec, J.-C., Dzikiti, S., Edgar, C., Eichstaedt, R., El-Madany, T. S., Elbers, J., Eller, C. B., Euskirchen, E. S., Ewers, B., Fonti, P., Forner, A., Forrester, D. I., Freitas, H. C., Galvagno, M., Garcia-Tejera, O., Ghimire, C. P., Gimeno, T. E., Grace, J., Granier, A., Griebel, A., Guangyu, Y., Gush, M. B., Hanson, P. J., Hasselquist, N. J., Heinrich, I., Hernandez-Santana, V., Herrmann, V., Hölttä, T., Holwerda, F., Irvine, J., Isarangkool Na Ayutthaya, S., Jarvis, P. G., Jochheim, H., Joly, C. A., Kaplick, J., Kim, H. S., Klemedtsson, L., Kropp, H., Lagergren, F., Lane, P., Lang, P., Lapenas, A., Lechuga, V., Lee, M., Leuschner, C., Limousin, J.-M., Linares, J. C., Linderson, M.-L., Lindroth, A., Llorens, P., López-Bernal, Á., Loranty, M. M., Lüttschwager, D., Macinnis-Ng, C., Maréchaux, I., Martin, T. A., Matheny, A., McDowell, N., McMahon, S., Meir, P., Mészáros, I., Migliavacca, M., Mitchell, P., Mölder, M., Montagnani, L., Moore, G. W., Nakada, R., Niu, F., Nolan, R. H., Norby, R., Novick, K., Oberhuber, W., Obojes, N., Oishi, A. C., Oliveira, R. S., Oren, R., Ourcival, J.-M., Paljakka, T., Perez-Priego, O., Peri, P. L., Peters, R. L., Pfautsch, S., Pockman, W. T., Preisler, Y., Rascher, K., Robinson, G., Rocha, H., Rocheteau, A., Röll, A., Rosado, B. H. P., Rowland, L., Rubtsov, A. V., Sabaté, S., Salmon, Y., Salomón, R. L., Sánchez-Costa, E., Schäfer, K. V. R., Schuldt, B., Shashkin, A., Stahl, C., Stojanović, M., Suárez, J. C., Sun, G., Szatniewska, J., Tatarinov, F., Tesař, M., Thomas, F. M., Tor-ngern, P., Urban, J., Valladares, F., van der Tol, C., van Meerveld, I., Varlagin, A., Voigt, H., Warren, J., Werner, C., Werner, W., Wieser, G., Wingate, L., Wullschleger, S., Yi, K., Zweifel, R., Steppe, K., Mencuccini, M., and Martínez-Vilalta, J.: Global transpiration data from sap flow measurements: the SAPFLUXNET database, Earth Syst. Sci. Data, 13, 2607–2649, https://doi.org/10.5194/essd-13-2607-2021, 2021.

Raghav, P., Kumar, M., and Liu, Y.: Structural constraints in current stomatal conductance models preclude accurate estimation of evapotranspiration and its partitions, Water Resour. Res., 60, e2024WR037652, https://doi.org/10.1029/2024WR037652, 2023.

Ramya, A., Dhevagi, P., Poornima, R., Avudainayagam, S., Watanabe, M., and Agathokleous, E.: Effect of ozone stress on crop productivity: A threat to food security, Environ. Res., 236, 116816, https://doi.org/10.1016/j.envres.2023.116816, 2023.

Ran, L., Pleim, J., Song, C., Band, L., Walker, J. T., and Binkowski, F. S.: A photosynthesis-based two-leaf canopy stomatal conductance model for meteorology and air quality modeling with WRF/CMAQ PX LSM, J. Geophys. Res.-Atmos., 122, 1930–1952, https://doi.org/10.1002/2016JD025583, 2017.

Rannik, Ü., Altimir, N., Mammarella, I., Bäck, J., Rinne, J., Ruuskanen, T. M., Hari, P., Vessala, T., and Kulmala, M.: Ozone deposition into a boreal forest over a decade of observations: evaluating deposition partitioning and driving variables, Atmospheric Chemistry and Physics, 12(24), 12165–12182, https://doi.org/10.5194/acp-12-12165-2012, 2012.

Savi, F. and Fares, S.: Ozone dynamics in a Mediterranean Holm oak forest: comparison among transition periods characterized by different amounts of precipitation, Annals of Silvicultural Research, 38, 1–6, https://doi.org/10.12899/ASR-801, 2014

Savi, F., Nemitz, E., Coyle, M., Aitkenhead, M., Frumau, K., Gerosa, G., Finco, A., Gruening, C., Goded, I., Loubet, B., Stella, P., Ruuskanen, T., Weidinger, T., Horvath, L., Zenone, T., and Fares, S.: Neural network analysis to evaluate ozone damage to vegetation under different climatic conditions. Frontiers in Forests and Global Change, 3, 42, https://doi.org/10.3389/ffgc.2020.00042, 2020.

Schröder, S., Schultz, M. G., Selke, N., Sun, J., Ahring, J., Mozaffari, A., Romberg, M., Epp, E., Lensing, M., Apweiler, S., Leufen, L. H., Betancourt, C., Hagemeier, B., and Rajveer, S.: TOAR Data Infrastructure, FZ-Juelich B2SHARE [data set], https://doi.org/10.34730/4d9a287dec0b42f1aa6d244de8f19eb3, 2021.

Schucht, S., Tognet, F., and Létinois, L.: Wheat yield loss in 2019 in Europe due to ozone exposure, Eionet Report-ETC/ATNI, https://www.eionet.europa.eu/etcs/etc-atni/products/etc-atni-report-17-2021-wheat-yield-loss-in-2019-in-europe-due-to-ozone-exposure (last access: 23 October 2024), 2021.

Schultz, M. G., Schröder, S., Lyapina, O., Cooper, O., Galbally, I., Petropavlovskikh, I., von Schneidemesser, E., Tanimoto, H., Elshorbany, Y., Naja, M., Seguel, R. J., Dauert, U., Eckhardt, P., Feigenspan, S., Fiebig, M., Hjellbrekke, A.-G., Hong, Y.-D.,

Kjeld, P. C., Koide, H., Lear, G., Tarasick, D., Ueno, M., Wallasch, M., Baumgardner, D., Chuang, M.-T., Gillett, R., Lee, M., Molloy, S., Moolla, R., Wang, T., Sharps, K., Adame, J. A., Ancellet, G., Apadula, F., Artaxo, P., Barlasina, M. E., Bogucka, M., Bonasoni, P., Chang, L., Colomb, A., Cuevas-Agulló, E., Cupeiro, M., Degorska, A., Ding, A., Fröhlich, M., Frolova, M., Gadhavi, H., Gheusi, F., Gilge, S., Gonzalez, M. Y., Gros, V., Hamad, S. H., Helmig, D., Henriques, D., Hermansen, O., Holla, R., Hueber, J., Im, U., Jaffe, D. A., Komala, N., Kubistin, D., Lam, K.-S., Laurila, T., Lee, H., Levy, I., Mazzoleni, C., Mazzoleni, L. R., McClure-Begley, A., Mohamad, M., Murovec, M., Navarro-Comas, M., Nicodim, F., Parrish, D., Read, K. A., Reid, N., Ries, L., Saxena, P., Schwab, J. J., Scorgie, Y., Senik, I., Simmonds, P., Sinha, V., Skorokhod, A. I., Spain, G., Spangl, W., Spoor, R., Springston, S. R., Steer, K., Steinbacher, M., Suharguniyawan, E., Torre, P., Trickl, T., Weili, L., Weller, R., Xiaobin, X., Xue, L., and Zhiqiang, M. : Tropospheric Ozone Assessment Report: Database and metrics data of global surface ozone observations, Elem Sci Anth, 5, 58, https://doi.org/10.1525/elementa.244, 2017.

Silva, S. J. and Heald, C. L.: Investigating dry deposition of ozone to vegetation, J. Geophys. Res.-Atmos., 123, 559–573, https://doi.org/10.1002/2017JD027278, 2018.

Simpson, D., Benedictow, A., Berge, H., Bergström, R., Emberson, L. D., Fagerli, H., Flechard, C. R., Hayman, G. D., Gauss, M., Jonson, J. E., Jenkin, M. E., Nyíri, A., Richter, C., Semeena, V. S., Tsyro, S., Tuovinen, J.-P., Valdebenito, Á., and Wind, P.: The EMEP MSC-W chemical transport model – technical description, Atmos. Chem. Phys., 12, 7825–7865, https://doi.org/10.5194/acp-12-7825-2012, 2012.

Sofen, E. D., Bowdalo, D., Evans, M. J., Apadula, F., Bonasoni, P., Cupeiro, M., Ellul, R., Galbally, I. E., Girgzdiene, R., Luppo, S., Mimouni, M., Nahas, A. C., Saliba, M., and Tørseth, K.: Gridded global surface ozone metrics for atmospheric chemistry model evaluation, Earth Syst. Sci. Data, 8, 41–59, https://doi.org/10.5194/essd-8-41-2016, 2016.

Stella, P., Personne, E., Loubet, B., Lamaud, E., Ceschia, E., Béziat, P., Bonnefond, J. M., Irvine, M., Keravec, P., Mascher, N., and Cellier, P.: Predicting and partitioning ozone fluxes to maize crops from sowing to harvest: the Surfatm-O_3 model, Biogeosciences, 8, 2869–2886, https://doi.org/10.5194/bg-8-2869-2011, 2011.

Stella, P., Personne, E., Lamaud, E., Loubet, B., Trebs, I., and Cellier, P.: Assessment of the total, stomatal, cuticular, and soil 2 year ozone budgets of an agricultural field with winter wheat and maize crops, J. Geophys. Res.-Biogeo., 118, 1120–1132, https://doi.org/10.1002/jgrg.20094, 2013.

Sun, S., Tai, A. P. K., Yung, D. H. Y., Wong, A. Y. H., Ducker, J. A., and Holmes, C. D.: Influence of plant ecophysiology on ozone dry deposition: comparing between multiplicative and photosynthesis-based dry deposition schemes and their responses to rising CO_2 level, Biogeosciences, 19, 1753–1776, https://doi.org/10.5194/bg-19-1753-2022, 2022.

Tai, A. P. K., Yung, D. H. Y., and Lam, T.: Terrestrial Ecosystem Model in R (TEMIR) version 1.0: simulating ecophysiological responses of vegetation to atmospheric chemical and meteorological changes, Geosci. Model Dev., 17, 3733–3764, https://doi.org/10.5194/gmd-17-3733-2024, 2024.

Tarasick, D., Galbally, I. E., Cooper, O. R., Schultz, M. G., Ancellet, G., Leblanc, T., Wallington, T. J., Ziemke, J., Liu, X., Steinbacher, M., Staehelin, J., Vigouroux, C., Hannigan, J. W., García, O., Foret, G., Zanis, P., Weatherhead, E., Petropavlovskikh, I., Worden, H., Osman, M., Liu, J., Chang, K. L., Gaudel, A., Lin, M., Granados-Muñoz, M., Thompson, A. M., Oltmans, S. J., Cuesta, J., Dufour, G., Thouret, V., Hassler, B., Trickl, T., and Neu, J. L. : Tropospheric Ozone Assessment Report: Tropospheric ozone from 1877 to 2016, observed levels, trends and uncertainties, Elementa: Science of the Anthropocene, https://doi.org/10.1525/elementa.376, 2019.

Travis, K. R. and Jacob, D. J.: Systematic bias in evaluating chemical transport models with maximum daily 8 h average (MDA8) surface ozone for air quality applications: a case study with GEOS-Chem v9.02, Geosci. Model Dev., 12, 3641–3648, https://doi.org/10.5194/gmd-12-3641-2019, 2019.

UNECE LRTAP: III. Mapping critical levels for vegetation, https://icpvegetation.ceh.ac.uk/sites/default/files/FinalnewChapter3v4Oct2017_000.pdf (last access: 14 October 2024), 2017

Visser, A. J., Ganzeveld, L. N., Goded, I., Krol, M. C., Mammarella, I., Manca, G., and Boersma, K. F.: Ozone deposition impact assessments for forest canopies require accurate ozone flux partitioning on diurnal timescales, Atmos. Chem. Phys., 21, 18393–18411, https://doi.org/10.5194/acp-21-18393-2021, 2021.

Walker, A. P., Quaife, T., Van Bodegom, P. M., De Kauwe, M. G., Keenan, T. F., Joiner, J., Lomas, M. R., MacBean, N., Xu, C., Yang, X., and Woodward, F. I.: The impact of alternative trait-scaling hypotheses for the maximum photosynthetic carboxylation rate ($V_{C_{\max}}$) on global gross primary production, New Phytologist, 215, 1370–1386, https://doi.org/10.1111/nph.14623, 2017.

Wang, T., Wang, F., Song, H., Zhou, S., Ru, X., and Zhang, H.: Maize yield reduction and economic losses caused by ground-level ozone pollution with exposure-and flux-response relationships in the North China Plain, J. Environ. Manage., 324, 116379. https://doi.org/10.1016/j.jenvman.2022.116379, 2022.

Wilkinson, M. D., Dumontier, M., Aalbersberg, I. J., Appleton, G., Axton, M., Baak, A., Blomberg, N., Boiten, J.-W., da Silva Santos, L. B., Bourne, P. E., Bouwman, J., Brookes, A. J., Clark, T., Crosas, M., Dillo, I., Dumon, O., Edmunds, S., Evelo, C. T., Finkers, R., Gonzalez-Beltran, A., Gray, A. J. G., Groth, P., Goble, C., Grethe, J. S., Heringa, J., 't Hoen, P. A. C., Hooft, R., Kuhn, T., Kok, R., Kok, J., Lusher, S. J., Martone, M. E., Mons, A., Packer, A. L., Persson, B., Rocca-Serra, P., Roos, M., van Schaik, R., Sansone, S.-A., Schultes, E., Sengstag, T., Slater, T., Strawn, G., Swertz, M. A., Thompson, M., van der Lei, J.,van Mulligen, E., Velterop, J., Waagmeester, A., Wittenburg, P., Wolstencroft, K., Zhao, J., and Mons, B.: The FAIR Guiding Principles for scientific data management and stewardship, Sci. Data, 3, 1–9, https://doi.org/10.1038/sdata.2016.18, 2016.

Wong, A. Y. H., Geddes, J. A., Ducker, J. A., Holmes, C. D., Fares, S., Goldstein, A. H., Mammarella, I., and Munger, J. W.: New evidence for the importance of non-stomatal pathways in ozone deposition during extreme heat and dry anomalies, Geophys. Res. Lett., 49, e2021GL095717, https://doi.org/10.1029/2021GL095717, 2022.

Wu, Z. Y., Wang, X. M., Chen, F., Turnipseed, A. A., Guenther, A. B., Niyogi, D., Charusombat, U., Xia, B. C., Munger, J. W.,

and Alapaty, K.: Evaluating the calculated dry deposition velocities of reactive nitrogen oxides and ozone from two community models over a temperate deciduous forest, Atmos. Environ., 45, 2663–2674, 2011.

Yen, M.-Ch., Peng, C.-M., Chen, T.-C., Chen, Ch.-S., Lin, N.-H., Tzeng, R.-Y., Lee, Y.-A., and Lin, Ch.-Ch.: Climate and weather characteristics in association with the active fires in northern Southeast Asia and spring air pollution in Taiwan during 2010 7-SEAS/Dongsha Experiment, Atmos. Environ., 78, 35–50, https://doi.org/10.1016/j.atmosenv.2012.11.015, 2013.

Yue, X. and Unger, N.: Ozone vegetation damage effects on gross primary productivity in the United States, Atmos. Chem. Phys., 14, 9137–9153, https://doi.org/10.5194/acp-14-9137-2014, 2014.

Yue, X., Keenan, T. F., Munger, W., and Unger, N.: Limited effect of ozone reductions on the 20-year photosynthesis trend at Harvard forest, Global Change Biology, 22, 3750–3759, https://doi.org/10.1111/gcb.13300, 2016.

Zhang, L., Brook, J. R., and Vet, R.: On ozone dry deposition—with emphasis on non-stomatal uptake and wet canopies, Atmospheric Environment, 36, 4787–4799, https://doi.org/10.1016/S1352-2310(02)00567-8, 2002.

Zhang, L., Brook, J. R., and Vet, R.: A revised parameterization for gaseous dry deposition in air-quality models, Atmos. Chem. Phys., 3, 2067–2082, https://doi.org/10.5194/acp-3-2067-2003, 2003.

Zhang, W., Feng, Z., Wang, X., Liu, X., and Hu, E.: Quantification of ozone exposure-and stomatal uptake-yield response relationships for soybean in Northeast China, Sci. Total Environ., 599, 710–720, https://doi.org/10.1016/j.scitotenv.2017.04.231, 2017.